# Effect of ternary additions of Cu and Fe on the hot deformation behavior of NiTi shape memory alloy - A study using processing maps

Author links open overlay panel Niraj Nayan [a], Gaurav Singh [b], S.V.S. Narayana Murty [a], P. Ramesh Narayan [a], M. Mohan [a], P.V. Venkitakrishnan [a], Upadrasta Ramamurty [c] [d]

[a] Vikram Sarabhai Space Center, Trivandrum, 695 022, India

[b] L3 Block, MEBP, Bangalore 560045, India

[c] School of Mechanical and Aerospace Engineering, Nanyang Technological University, Singapore, 639798, Republic of Singapore

[d] Institute of Materials Research and Engineering, Agency for Science, Technology and Research (A∗STAR), Singapore, 138634, Republic of Singapore

## Abstract

The addition of ternary alloying elements Cu and Fe on the hot workability of binary NiTi SMA is assessed using the processing maps approach. Uniaxial compression test data obtained in the temperature, $T$, range 800–1050 °C and strain rate, $\dot{\varepsilon}$, of $10^{-3}$ – $10^{+1}$ $s^{-1}$ were utilized to construct power dissipation, instability and strain rate sensitivity maps at true strain, $\varepsilon = 0.5$. These maps and complementary microstructural analyses of the deformed specimens were used to identify various deformation mechanisms operating in different $T$- $\dot{\varepsilon}$ regimes. Based on the processing maps, three stable domains for processing were identified with Domain-2 occurring at higher $T$ and intermediate $\dot{\varepsilon}$ with power dissipation efficiency of 30–45% being the optimum for thermo-mechanical processing. The addition of Cu in NiTi SMA improves its hot workability through enlarging stable domains for processing whereas Fe addition shrinks it. Microstructural analysis indicates occurrence of dynamic recrystallization (DRX) in NiTi, NiTiFe and dynamic recovery (DRV) in NiTiCu as the dominating deformation mechanism in Domain-2. Sluggish DRX kinetics in NiTiCu SMA in Domain-2 is related to its higher deformation resistance and higher critical stress required for the onset of DRX vis-à-vis NiTi, NiTiFe SMAs. Instability maps corroborated through microstructural analysis showed instability in the form of flow localization.

Keywords
Hot deformation; Shape memory alloy; Shape memory effect; Superelasticity; Martensite; Dynamic recrystallization

## 1. Introduction

SMAs exhibit either shape memory effect (SME) or superelasticity (SE) due to thermoelastic-martensitic transformation from the high temperature B2 austenite phase to low temperature B19' martensite phase [[1], [2], [3]]. Binary NiTi SMAs are extensively used in many aerospace and biomedical applications due to their unique characteristics of superior SME and higher SE as compared to any other alloys of this family [4,5]. The shape memory characteristics of them can be modified by the addition of ternary alloying elements chemically equivalent to Ni or Ti [6]. Some of the common alloying elements are Cu, Fe, Nb, Co, Hf, Pd, Pt and Zr [[7], [8], [9], [10], [11]]. For example, the substitution of Nb for Ni increases the phase transformation temperature hysteresis [12] whereas the addition of Co alters its phase transformation temperature, microstructure and magnetic properties [13,14]. The additions of Hf, Pd, Pt and Zr increase the reverse transformation temperature and make NiTi suitable for high temperature shape memory applications [[8], [9], [10]]. The addition of Cu to binary NiTi SMA increases its thermoelastic response, decreases the hysteresis loss and the yield strength of the martensite phase, reduces the composition sensitivity of the martensite start temperature [3,[15], [16], [17], [18], [19]]. Furthermore, it improves the thermal fatigue and actuation responses, and prevents the precipitation of $Ni_3Ti_4$ phase [3,[20], [21], [22], [23], [24]]. This makes the NiTiCu SMA a preferred choice for actuator applications as compared to the binary NiTi SMA [25]. The addition of Fe to NiTi results in the lowering of the martensitic transformation temperature along with the introduction of an intermediate trigonal R-phase [[26], [27], [28], [29]]. The transformation of cubic austenite to trigonal R−phase in NiTiFe alloy results in a lower hysteresis loss and hence an improved fatigue response [30]. Moreover, this takes place in lower temperature range [29,31]. The NiTiFe SMA is typically used in coupling applications due to its lower martensite transformation start temperature [26,27]. Therefore, Cu and Fe as ternary alloying elements are promising in widening the application potential of the NiTi based SMAs.

For majority of the applications like in actuators, valves, couplings, and biomedical implants, the NiTi based SMAs are used in the form of wires, tubes, or thin sheets. The smaller final size of the components necessitates several thermo-mechanical processing steps to reduce the as-cast ingots to the required sizes. Also, hot working methods like rolling, forging, extrusion, and drawing are essential for producing high quality semi-finished products of the NiTi alloys. Therefore, identification of the optimum thermo-mechanical processing steps and the combinations of parameters such as $T$, $\dot{\varepsilon}$ and $\varepsilon$ to be employed for obtaining the desired microstructures is essential. The latter is particularly relevant in the context of SMAs as their functional properties are highly sensitive to the underlying microstructure.

The hot deformation behaviors of NiTi family of SMAs have been studied extensively in the past [[32], [33], [34], [35], [36], [37], [38], [39], [40], [41]]. Even though, NiTiCu and NiTiFe SMAs are possible contenders to replace the binary NiTi SMA in various engineering applications, literature on the hot deformation behavior of these materials is limited. Shastry et al. [42] studied the hot deformation behavior of $Ni_{42}Ti_{50}Cu_{8}$ (at.%[1]) SMA in the $T$ range of 800–1050 °C and $\dot{\varepsilon} = 10^{-3}$ -$10^{+2}$ $s^{-1}$. Their results show that the safe hot working zone for the alloy are in the range $T$ = 800–850 °C and $\dot{\varepsilon} = 10^{-1.5}$ - $10^{-0.5}$ $s^{-1}$, wherein the grain refinement through DRX mechanism is dominant. The occurrence of DRX was also confirmed during hot tensile tests of NiTiCu SMA [43]. The maximum ductility due to DRX was observed in the $T$ range of 800–1000 °C and $\dot{\varepsilon}$ = 0.1 $s^{-1}$ [43]. Zhang et al. [44] studied the hot deformation behavior and processing map of $Ni_{45}Ti_{50}Cu_{5}$ SMA with an starting acicular martensitic microstructure in the $T$ range of 600–1000 °C and $\dot{\varepsilon} = 5 \times 10^{-4}$ - 0.5 $s^{-1}$ and reported an optimum hot working zone at $T$ = 750–850 °C and $\dot{\varepsilon} = 5 \times 10^{-4}$ – $10^{-3}$ $s^{-1}$. It is clear from the above two works that the optimum hot working zone is highly sensitive to Cu content in NiTiCu SMA. Morakabati et al. [45] examined the influence of the Cu addition on the deformation behavior of $Ti_{50.4}Ni_{49.6-x}Cu_{x}$ ($x$ = 0, 3, 5 and 7 at.%) through hot compression tests in the $T$ range 700–1000 °C and $\dot{\varepsilon}$ = 0.1 $s^{-1}$. They reported an increase in the critical stress required for the onset of DRX and work hardening rate with increasing Cu content. This was attributed to solid solution strengthening caused by substitution of Ni with Cu and precipitation hardening from Cu containing precipitates in higher Cu content alloys ($x \geq 5$ at.%) [45]. Basu et al. [46] investigated microstructure evolution after hot compression testing of $Ni_{47}Ti_{50}Fe_{3}$ SMA in the $T$ range of 750–950 °C and $\dot{\varepsilon}$ of 10 and 100 $s^{-1}$. The deformed microstructures of $Ni_{47}Ti_{50}Fe_{3}$ SMA showed grain boundary serrations along with the occurrence of DRX that results in fine equiaxed grains. It was reported that the increased fraction of DRX grains suppress austenite to martensite phase transformation [46]. Shujuan and co-workers [47] studied the hot deformation behavior of $Ni_{47}Ti_{50}Fe_{3}$ SMA with the aid of processing map generated in the $T$ range of 750–1050 °C and $\dot{\varepsilon} = 10^{-2}$ – $10^{+1}$ $s^{-1}$ and found that the flow instability regions increase with an increase in $\varepsilon$. The optimum hot working zone for processing was identified as $T$ = 950–1050 °C and $\dot{\varepsilon} = 10^{-2}$ – $10^{-1}$ $s^{-1}$.

Processing maps are effective and reliable tools to determine the optimum processing parameters ($T$ and $\dot{\varepsilon}$) that control the final microstructure of the component, increasing productivity and reducing lead time by avoiding trial and error during manufacturing [48]. In the present work, we utilize the processing maps approach for assessing the effect of Cu and Fe addition on the hot workability of NiTi SMA, in terms of expanding or contracting the stable regime for processing. The processing maps are constructed based on the modified dynamic material model (DMM) proposed by Murty and Rao [49,50]. As already mentioned, there are already few reported works on the processing maps of NiTiCu [42,44] and NiTiFe [47] SMAs, however the Cu and Fe content examined in these works are different from the present study. Since a marginal change in the chemical composition or processing route can have a significant influence on the final microstructure, as functional and mechanical properties are strongly dependent on microstructure and grain size [3,51]. Another objective of the present work is to determine the constitutive behavior of the SMAs during plastic flow. For these purposes, a series of hot compression tests are conducted in the $T$ range of 800–1050 °C and $\dot{\varepsilon}$ = $10^{-3}$ – $10^{+1}$ $s^{-1}$. The constructed maps of the SMAs were utilized to identify various domains of safe and unsafe regimes for processing in the $T$- $\dot{\varepsilon}$ space.

## 2. Theory behind the processing map approach

In this section, the scientific basis for the construction of processing map is briefly explained. Readers are referred to Refs. [42,48,[52], [53], [54], [55], [56], [57]] for more details. According to the DMM that underpins this approach, the material that is being deformed acts as a non-linear power dissipater. The total power per unit volume, *P*, can be partitioned into of two complementary parts, *G* and *J*:

$$(1)\ \mathrm{P{=}G{+}J{=}\sigma\varepsilon{=}}\ \int_0^{\dot{\varepsilon}} \sigma\, \partial\, \dot{\varepsilon} + \int_0^{\sigma} \dot{\varepsilon}\ \partial\sigma$$

The *G* content is related to power dissipated through plastic deformation, majority of which is converted into heat. The *J* content, which is complementary to the G content, is related to power dissipated through microstructural changes. The factor that partitions the power between the *G* and *J* contents is the strain rate sensitivity, *m*, of the flow stress, given by

$$(2)\ \sigma{=}\mathrm{K}(\dot{\varepsilon})^{m}$$

where $\sigma$ is flow stress and *K* is constant. From Eqs [1]. and [2],

$$(3)\left[\frac{\partial J}{\partial G}\right]_{\dot{\varepsilon},\mathrm{T}} = \left[\frac{\dot{\varepsilon}\,\partial\sigma}{\sigma\,\partial\dot{\varepsilon}}\right]_{\dot{\varepsilon},\mathrm{T}} = \left[\frac{\partial(\ln\sigma)}{\partial(\ln\dot{\varepsilon})}\right]_{\dot{\varepsilon},\mathrm{T}} = m.$$

The *J* content is given by:

$$(4)\mathrm{J} = \frac{m\sigma\dot{\varepsilon}}{m+1}$$

Since the value of *m* varies from 0 to 1; when $m = 0$, $J = 0$ and $m = 1$, $J = G$. For an ideal linear power dissipater, $m = 1$ and $J = J_{max}$. The efficiency of power dissipation, $\eta$, which is obtained by normalizing *J* with $J_{max}$ and is given as:

$$(5)\eta = \frac{J}{J\mathrm{max}} = \frac{2m}{m+1}$$

A modified version of DMM was proposed by Murty and Rao [49,50] in which the value of *m* at constant $\varepsilon$ and *T* varies with $\dot{\varepsilon}$ and it becomes independent of $\dot{\varepsilon}$ if $\sigma$ and $\dot{\varepsilon}$ follows power-law according to Eq [2]. This is in contrast to Prasad et al.'s [48] model where *m* is independent of $\dot{\varepsilon}$. Since power-law behavior is valid only at lower $\dot{\varepsilon}$, the method for the estimation for *J* was subsequently modified by Murty and Rao,

$$(6) J = P{-}G = \sigma\dot{\varepsilon} - \int_0^{\dot{\varepsilon}} \sigma \mathrm{d}\dot{\varepsilon}$$

$$(7)\eta = \frac{J}{J_{max}} = \frac{2(\mathrm{P}-\mathrm{G})}{\sigma\dot{\varepsilon}} = 2\left(1 - \frac{1}{\sigma\dot{\varepsilon}}\int_{10^{-3}}^{\dot{\varepsilon}} \sigma \mathrm{d}\dot{\varepsilon}\right)$$

$$(8)\eta = 2\left[1 - \frac{1}{\sigma\dot{\varepsilon}}\left(\int_0^{10^{-3}} \sigma \mathrm{d}\dot{\varepsilon} + \int_{10^{-3}}^{\dot{\varepsilon}} \sigma \mathrm{d}\dot{\varepsilon}\right)\right]$$

The integral in Eq [7]. is split in two parts with $\dot{\varepsilon}$ limits from 0 to $10^{-3}\ s^{-1}$ and $10^{-3}\ s^{-1}$ to $\dot{\varepsilon}$. The first part of the integral in Eq [8]. is valid only up to a strain rate of $10^{-3}\ s^{-1}$ where it is assumed that $\sigma$ versus $\dot{\varepsilon}$ curve obeys power-law equation defined in Eq [2]. Eq [8]. further simplifies into:

$$(9)\eta = 2[1 - \frac{1}{\sigma\dot{\varepsilon}}[[\frac{\sigma\dot{\varepsilon}}{(m+1)}]_{\dot{\varepsilon}=10^{-3}} + \int_{10^{-3}}^{\dot{\varepsilon}} \sigma d\dot{\varepsilon})]]$$

The above Eq [9]. is solved numerically to obtain $\eta$ using cubic-spline interpolated $\sigma$ - $\dot{\varepsilon}$ data. The two-dimensional (2-D) contour map of $\eta$ in $T$ - $\dot{\varepsilon}$ space constitutes the power dissipation map. Here, $\eta$ represents the way in which material dissipates power through various metallurgical processes like DRV, DRX etc. during hot deformation.

Based on the maximum rate of entropy production, a flow instability criterion is defined in Ref. [58] and is used to delineate the flow instability regime. According to the criterion [59], flow instability is given by the equation:

$$(10)\varsigma(\dot{\varepsilon}) \frac{\partial \ln(\frac{m}{m+1})}{\partial \ln(\dot{\varepsilon})} + m < 0$$

where $\zeta(\dot{\varepsilon})$ is an dimensionless instability parameter and the variation of $\zeta(\dot{\varepsilon})$ with $T$ and $\dot{\varepsilon}$ constitutes an instability map. Regions in the instability map with $\zeta(\dot{\varepsilon})< 0$ indicate to microstructural instabilities in the form of flow localization, shear banding, wedge cracking, etc and should be avoided during processing of the material. It is important to mention that $\eta$ defined in Eq [5]. is only valid explicitly when the $\sigma$–$\varepsilon$ curve obeys power-law, i.e., $m$ is independent of $\dot{\varepsilon}$. However, $\eta$ and $\zeta(\dot{\varepsilon})$ can be computed for any type of flow curve using the procedures described in Ref. [60] and the same was followed in the present work for the generation of the instability maps.

As explained in Refs. [60,61], the criteria for the occurrence of metallurgical instability during deformation is described below:

$$(11)\frac{2m}{n-1} < 0$$

For material to exhibit stable flow, $0 < \eta < 2m$ and the range of $m$ values ($0 < m \leq 1$) are derived from the theoretical consideration of the maximum rate of power dissipation by material systems and experimental observations. The instability criterion derived in Eq [11]. is valid for any type of $\sigma$–$\varepsilon$ curve. Finally, the processing map is constructed by superimposing instability map on the power dissipation map.

## 3. Materials and experiments

Three SMAs with the nominal chemical compositions of $Ni_{50}Ti_{50}$, $Ni_{40.6}Ti_{55.2}Cu_{4.1}$ and $Ni_{48.5}Ti_{50.05}Fe_{1.43}$ (at.%) were prepared by vacuum arc melting process and are examined in the as-cast state. Here afterwards, the three SMAs will be referred as NiTi, NiTiCu and NiTiFe, respectively. Melting was performed in an Ar gas atmosphere using tungsten as the electrode with water-cooled Cu crucible as the hearth. High purity Ni (99.99%), Ti (99.97%), Cu (99.99%) and Fe (99.99%) were used as raw materials in appropriate proportions. The cast buttons, weighing ~350 g each, were flipped and re-melted six times to ensure melt homogeneity. The phase transformation temperatures $M_s$, $M_f$, $A_s$, $A_f$ ($M_s$ = Martensite transformation start temperature; $M_f$ = Martensite transformation finish temperature; $A_s$ = Reverse transformation start temperature; $A_f$ = Reverse transformation finish temperature) of NiTi, NiTiCu and NiTiFe SMAs were determined with the aid of differential scanning calorimetry (DSC) as per the ASTM F2004 standard. The DSC experiments (PI make, model Q 2000) were performed in the temperature range of 20–200 °C with the heating and cooling rates of 5 °C/min under Ar gas.

Cylindrical specimens that are 10 mm in diameter and 15 mm in height were used for the high temperature uniaxial compression tests. A hole of 0.8 mm diameter and 5 mm depth was spark drilled at midway height of the specimens to insert thermocouple. Compression tests were carried out on a computer-controlled servo-hydraulic machine (DARTEC, UK) equipped with split-type resistance heating furnace. The compression tests on NiTi and NiTiFe were conducted at temperatures, $T$, of 800, 900, 950, 1000 and 1050 °C while for NiTiCu at 800, 850, 900, 950, 1000 and 1050 °C. The specimens were pre-heated to the test temperature at a heating rate of 5 °C/s and held for 5 min to homogenize the temperature. At each temperature, tests were conducted at constant $\dot{\varepsilon}$ of $10^{-3}$, $10^{-2}$, $10^{-1}$, 1 and 10 $s^{-1}$ to true strain, $\varepsilon$, of ~ 0.7 (which corresponds to 50% height reduction). In order to minimize the frictional stresses generated during deformation, borosilicate lubricant was applied between the specimen and the platens. The temperature was monitored using Platinum/Platinum-Rhodium thermocouple attached to the specimen. The accuracy of the temperature control is within ±2 °C. After the hot-compression tests, all the deformed specimens were air-cooled to room temperature. The recorded load-stroke data was converted into true stress and true strain plots. The adiabatic temperature rise in specimens during deformation was found to be negligible and hence was not taken into account for correcting the flow stress.

The microstructures of as-cast and deformed specimens were characterized by optical microscopy. The hot deformed specimens were sectioned longitudinally in the direction parallel to the compression axis. The specimens were prepared for optical metallography using standard grinding and polishing procedures and etched with modified Kroll's reagent (10% HF + 15% $HNO_3$ + 75% $H_2O$).

## 4. Results and discussion

### 4.1. As-cast microstructures

The as-cast microstructures of the SMAs are shown in Fig. 1. As evident from them, the microstructures are homogeneous and exhibit no segregation. The grain morphology in NiTi and NiTiCu SMAs appears to be 'pancake' like while it is equiaxed in NiTiFe. High magnification imaging confirmed that the black spots in Fig. 1 are etch pits. It appears that the amount of Cu (4.1 at.%) and Fe (1.43 at.%) added in the present work are not sufficient to nucleate Fe and Cu rich precipitates in the NiTi matrix during direct cooling that occurs during the casting process.

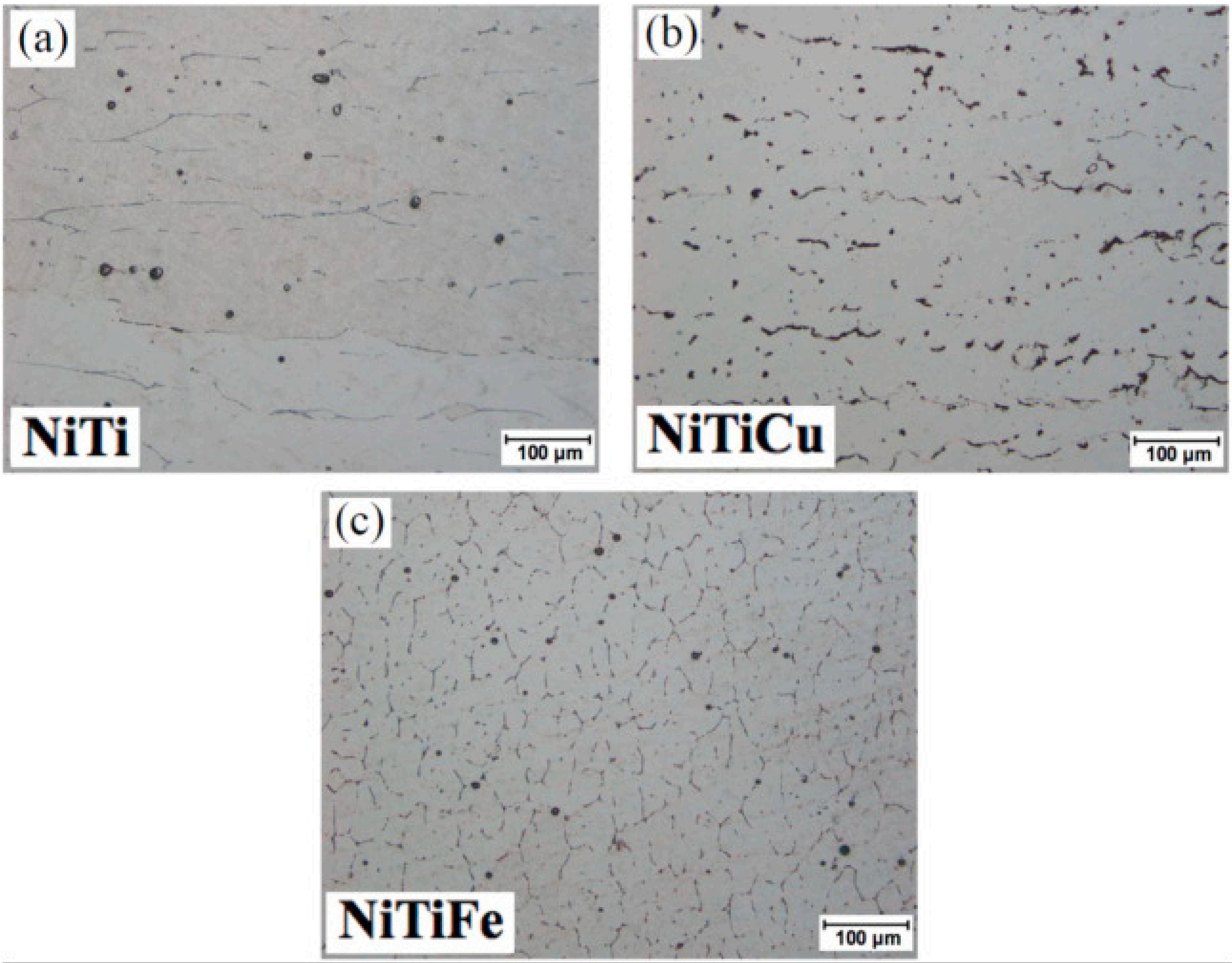


1. Download: Download high-res image (781KB)
2. Download: Download full-size image

Fig. 1. The as-cast microstructures of (a) NiTi, (b) NiTiCu and (c) NiTiFe SMAs.

## 4.2. Effect of Cu and Fe addition on the phase transformation temperatures

Fig. 2 shows the DSC scans obtained on NiTi, NiTiCu and NiTiFe SMAs in the as-cast condition. The transformation temperatures $M_s$, $M_f$, $A_s$ and $A_f$ temperatures determined from the scans are summarized in Table 1. It can be seen that $M_f$ of NiTi, NiTiCu and NiTiFe SMAs are 54.2, 45.3 and 49.3 °C respectively and are greater than room temperature (~22 °C). Thus, the investigated SMAs are martensitic at the room temperature. All the three SMAs exhibit a one-step phase transformation from B19′ martensite to B2 austenite during heating and reverse transformation during cooling in the investigated temperature range. While the addition of Cu and Fe to NiTi does not appear to change the phase transformation path, it affects the transformation temperatures; both $M_s$ and $M_f$ decreases with the Cu addition while no significant effect on the transformation temperatures was noted with Fe addition. Interestingly, the peak associated with the transformation of B2 austenite to B19’ martensite in NiTiCu during cooling diminishes considerably.

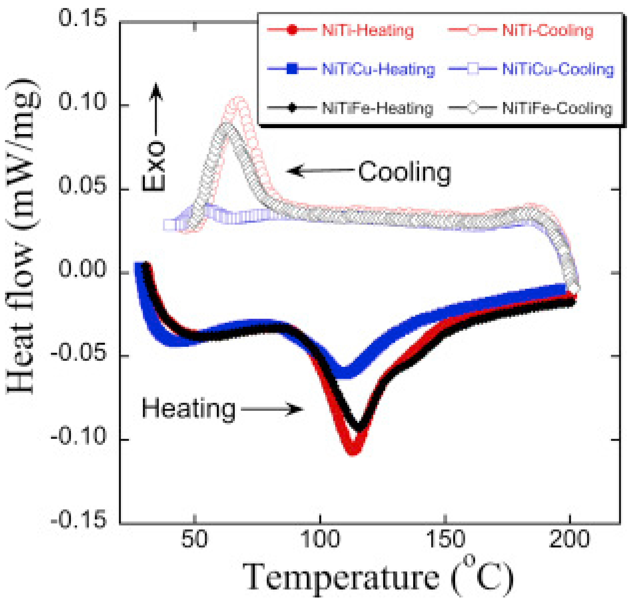


1. Download: Download high-res image (292KB)
2. Download: Download full-size image

Fig. 2. DSC curves of NiTi, NiTiCu and NiTiFe SMAs in as-cast condition. The phase transformation temperatures $M_s$, $M_f$, $A_s$, $A_f$ are listed in Table 1.

Table 1. Phase transformation temperatures of the investigated SMAs.

| Alloy | Phase transformation temperature (°C) | | | |
|---|---|---|---|---|
| | $M_f$ | $M_s$ | $A_s$ | $A_f$ |
| NiTi | 54.2 | 79.2 | 98.4 | 123.8 |

| Alloy | Phase transformation temperature (°C) | | | |
|---|---|---|---|---|
| | **$M_f$** | **$M_s$** | **$A_s$** | **$A_f$** |
| NiTiCu | 45.3 | 64.8 | 93.4 | 131.3 |
| NiTiFe | 49.3 | 77.7 | 96.5 | 123.8 |

The martensitic transformation temperature in SMAs depends upon the valency, atomic size and electronegativity of the alloying elements [1]. It is well established in the literature that Ni is more effective in changing it in comparison to Ti, Cu and Fe [1,3,11,62]. Increasing the Ni content stabilizes the martensite [62]. The addition of Cu (4.1 at.%) and Fe (1.43 at.%) reduces the overall Ni content from 50 at.% in the binary NiTi to 40.6 and 48.5 at.% in NiTiCu and NiTiFe, respectively. The reduction of the Ni content by ~9.4 at.% due to the addition of Cu results in the reduction of $M_s$ from 79.2 to 64.8 °C and $M_f$ from 54.2 to 45.3 °C, see Table 1. On the other hand, addition of 1.43 at.% Fe in NiTiFe SMA does not lead to any significant change in the concentration of Ni in comparison to binary NiTi.

## 4.3. Flow curves

In the present work, a large number of true stress ($\sigma$) - true strain ($\varepsilon$) responses were generated (three SMAs, a total of 80 $\sigma$-$\varepsilon$ curves). For the sake of brevity, only representative responses are shown in the main text. Rest are provided as Supplementary Information (SI). Representative $\sigma$-$\varepsilon$ responses of NiTi, NiTiCu and NiTiFe SMAs at different $T - \dot{\varepsilon}$ combinations are shown in Fig. S1, S2 and S3. As expected, $\sigma$ decreases with increasing $T$ and decreasing $\dot{\varepsilon}$. At lower strain rates $\dot{\varepsilon} \leq 1\ s^{-1}$, flow curves of the three SMAs exhibit a broad peak in flow stress at relatively low strain ($\varepsilon < 0.05$) followed by steady-state flow behavior at all the $T$. On the other hand, at the higher strain rate of $\dot{\varepsilon} = 10\ s^{-1}$, a marked drop in $\sigma$ after peak stress occurred followed by gradual flow softening. These behaviors indicate occurrence of DRV or DRX. At intermediate strain rates ($\dot{\varepsilon} = 10^{-2}$ - $1\ s^{-1}$), the plastic flow behavior is jerky in nature, similar to that reported in another SMA [47], where it results from competitions between work hardening and softening during deformation of the material. Multiple humps or double peak in the flow curves of the SMAs were observed at $\dot{\varepsilon} = 1\ s^{-1}$ (Fig. S1(d), S2(d) and S3(d)). These could be related to plastic flow instabilities. It is difficult to predict the dominant deformation mechanism solely on the basis of the flow responses. Consequently, microstructural analysis of the deformed specimens and processing maps are used to predict the operating deformation mechanisms, discussed in detail later.

Fig. 3 compares the flow responses of the NiTi, NiTiCu and NiTiFe SMAs obtained at $T = 800$ °C, $\dot{\varepsilon} = 10^{-2}\ s^{-1}$ and at $T = 1000$ °C, $\dot{\varepsilon} = 10\ s^{-1}$. As evident from them, flow stresses in the ternary NiTiCu and NiTiFe SMAs are higher in comparison to binary NiTi SMA. However, the shape of the flow curves remains invariant with the Cu and Fe addition in NiTi. The extent of enhancement in flow stress with Cu addition was more in comparison to Fe. Interestingly, the increase in flow stress with increasing $\varepsilon^{\cdot}$ was much higher in comparison to decreasing $T$.

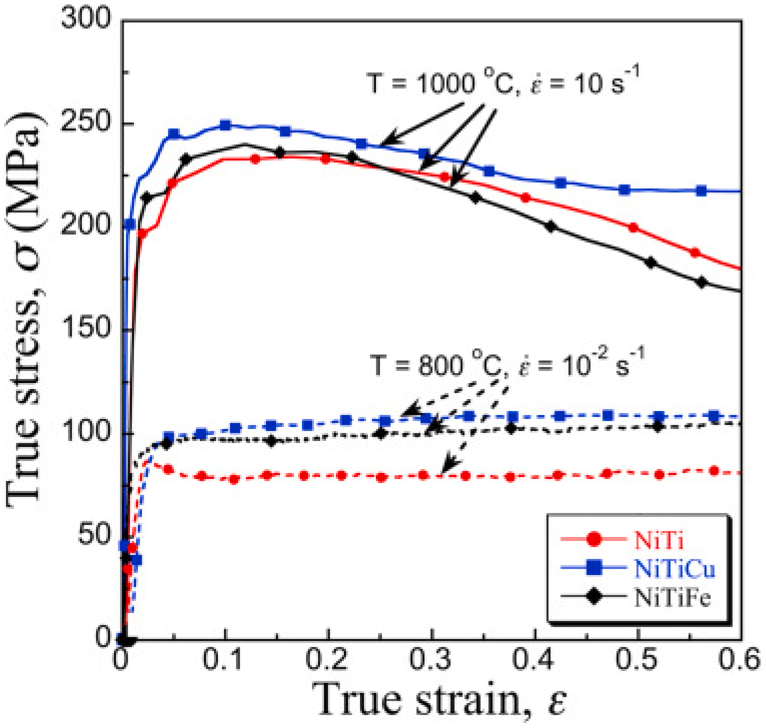


1. Download: Download high-res image (344KB)
2. Download: Download full-size image

Fig. 3. Comparison of flow curves of NiTi, NiTiCu and NiTiFe SMAs at $T$ = 800 °C, $\dot{\varepsilon} = 10^{-2}$ $s^{-1}$ (broken lines) and $T$ = 1000 °C, $\dot{\varepsilon}$ = 10 $s^{-1}$ (solid lines).

### 4.3.1. Yield stress

Representative variation of 0.2% yield stress, $\sigma_y$, at various $\dot{\varepsilon}$ for NiTiFe is plotted as a function of $T$ in Fig. 4a. The $\sigma_y$ at each $T$ and $\dot{\varepsilon}$ is normalized with $\sigma_y$ at 800 °C and corresponding $\dot{\varepsilon}$ (Fig. 4b. Similarly, the $\sigma_y$ obtained at each $\dot{\varepsilon}$ and $T$ is normalized with the $\sigma_y$ at $\dot{\varepsilon} = 10^{-3}$ $s^{-1}$ for corresponding $T$ (Fig. 4c). These normalized plots clearly show that the variation of $\sigma_y$ is monotonic in nature, i.e., $\sigma_y$ increases with increasing $1/T$ or $\dot{\varepsilon}$.

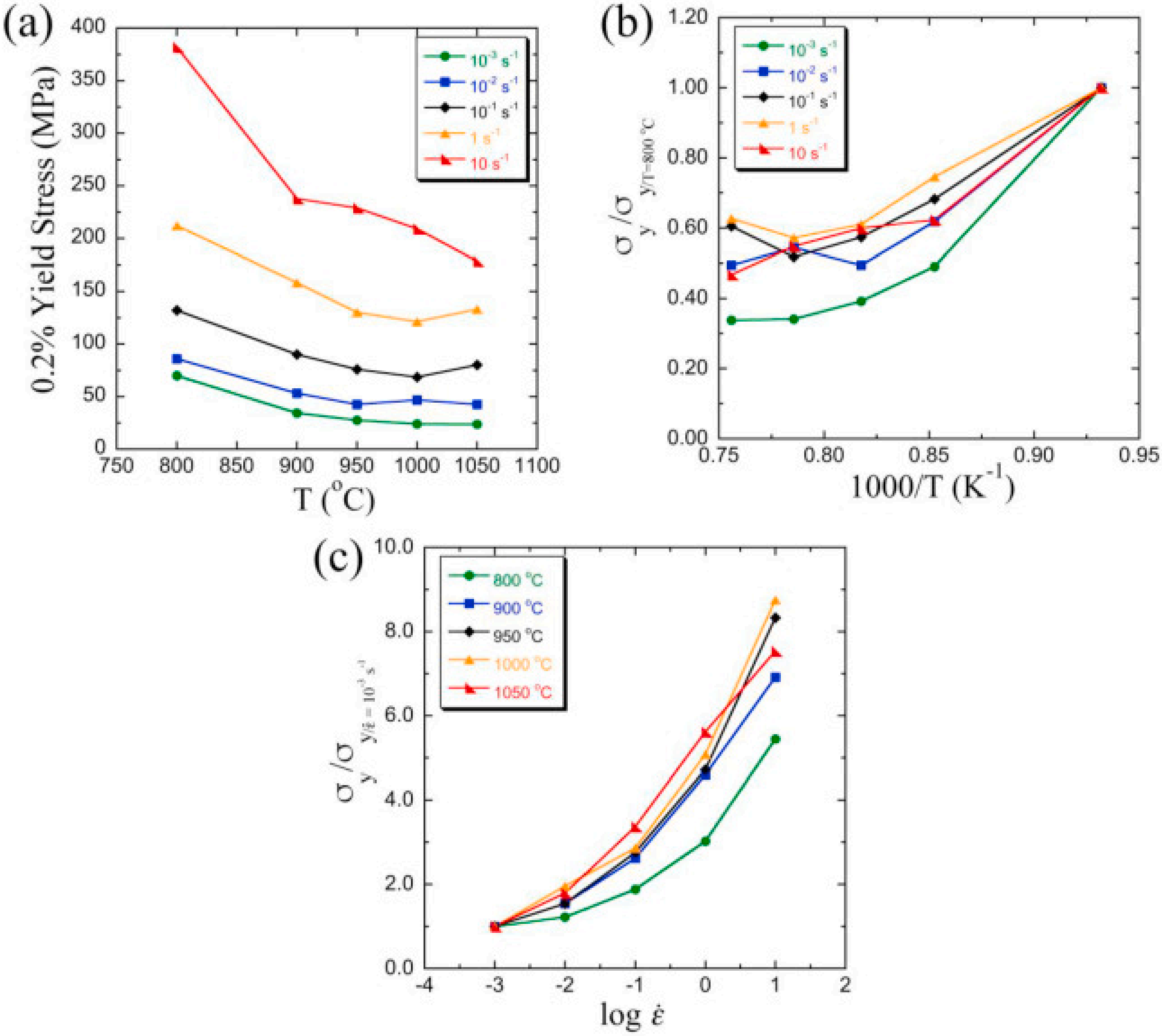


1. Download: Download high-res image (624KB)
2. Download: Download full-size image

Fig. 4. (a) Variation of $\sigma_y$ with $T$ and $\dot{\varepsilon}$ for NiTiFe SMA. Plots (b) and (c) are normalized $\sigma_y$ values with respect to $T$ and $\dot{\varepsilon}$ respectively.

---

## 4.4. Modeling of flow curves: Constitutive equations

### 4.4.1. Determination of materials constants

Results presented above clearly show that flow stresses of the examined SMAs during deformation are markedly affected by $\dot{\varepsilon}$, $\varepsilon$ and $T$. The inter-dependence of $\sigma$, $\dot{\varepsilon}$ and $T$ can be related using the constitutive equations, whose constants are determined from the test data. An Arrhenius type hyperbolic-sine equation is used to describe the high-temperature deformation behavior of the SMAs [63]:

$$(12)\ \dot{\varepsilon} = A[\sinh(\alpha\sigma)]^n \exp\left(\frac{-Q}{RT}\right),$$

where $Q$ is the activation energy of deformation, $n$ is the stress exponent, $A$, $\alpha$ and $\beta$ are experimentally determined constants with $\alpha = \beta/n$ [52,53] and $R$ is gas constant (8.314 J/mol-K).

The term $[sinh(\alpha\sigma)]^n$ can be further simplified as power-law or exponential form depending upon the value of $\alpha\sigma$:

$$(13)\ [\sinh(\alpha\sigma)]^n = \begin{cases} \sigma^n & \alpha\sigma < 0.8 \\ \exp(\beta\sigma) & \alpha\sigma > 1.2 \end{cases}$$

Combining Eqs [12]. and [13], we obtain

$$(14)\ \dot{\varepsilon} = A_1\, \sigma^n \exp\left(\frac{-Q}{RT}\right) \text{ or}$$

$$(15)\ \dot{\varepsilon} = A_2 \exp(\beta\sigma) \exp\left(\frac{-Q}{RT}\right)$$

The values $\beta$ and $n$ are estimated from the slopes of the ln $\dot{\varepsilon}$ vs. $\sigma$ and ln $\dot{\varepsilon}$ vs. ln $\sigma$ plots, respectively, with $\sigma$ data taken at $\varepsilon$ = 0.5 at each temperature. Representative plots for the NiTiFe SMA are shown in Fig. 5(a) and (b). Excellent linear fits between ln $\dot{\varepsilon}$ vs. ln $\sigma$ plots indicate that the values of $n$ at a fixed $T$ are independent $\dot{\varepsilon}$ but sensitive to $T$. Similar analysis were performed with the flow stress values obtained at $\varepsilon$ = 0.1, 0.2, 0.3 and 0.4; the observed trends and conclusions are broadly consistent with those obtained at $\varepsilon$ = 0.5. The values of $\alpha$ at $\varepsilon$ = 0.5 is estimated by using the average values of $\beta$ and $n$ at different $T$. The obtained values of $\alpha$ for NiTi, NiTiCu and NiTiFe SMAs are 0.0098, 0.0064 and 0.0091 MPa$^{-1}$, respectively.

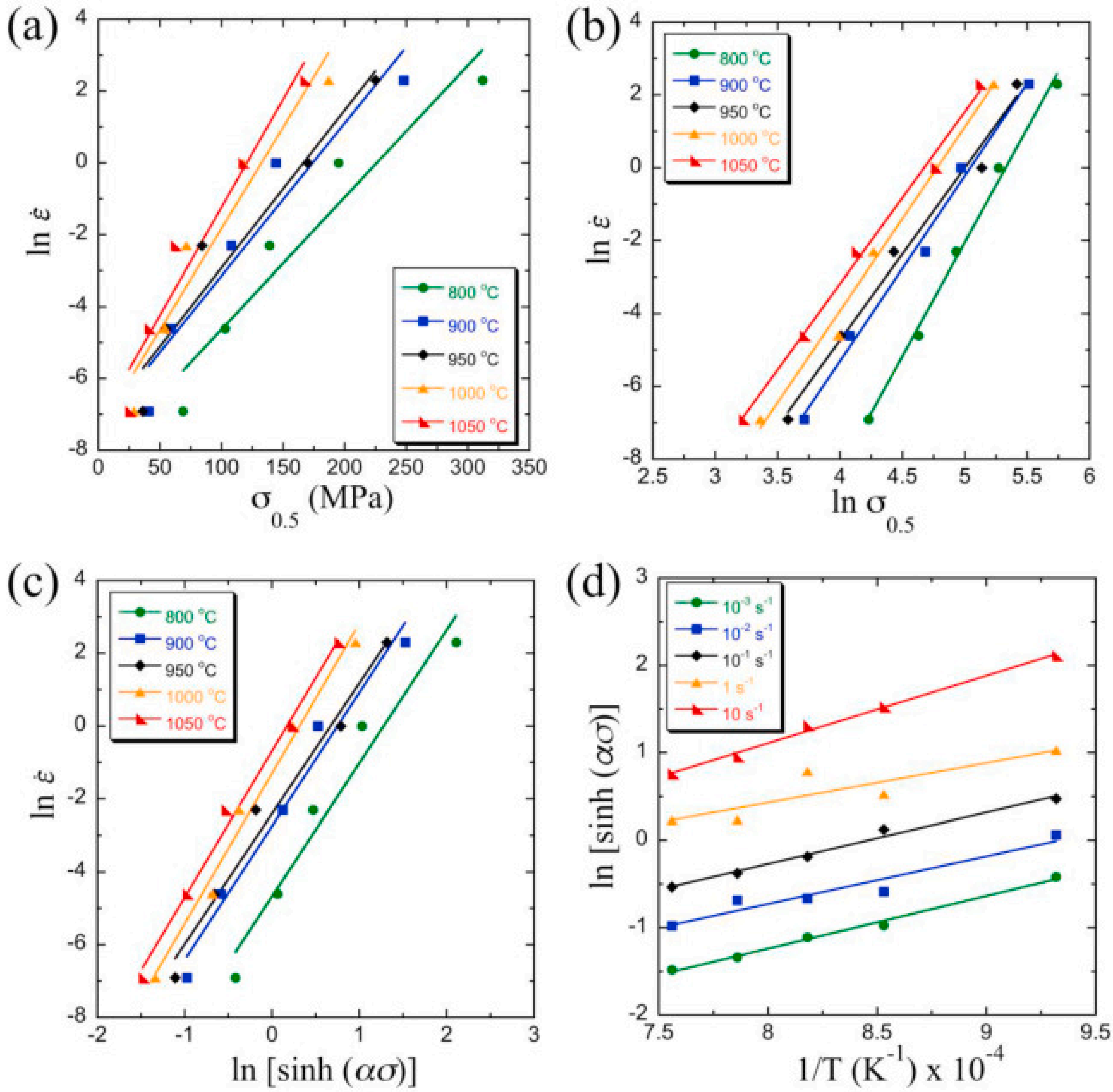


1. Download: Download high-res image (915KB)
2. Download: Download full-size image

Fig. 5. (a) $\ln \dot{\varepsilon}$ vs. $\sigma$ and (b) $\ln \dot{\varepsilon}$ vs. $\ln \sigma$ plots utilized for estimating $\beta$ and $n$; (c) $\ln \dot{\varepsilon}$ vs. $\ln [\sinh(\alpha\sigma)]$ and (d) $\ln [\sinh(\alpha\sigma)]$ vs. $1/T$ plots utilized for the estimation of activation energy, $Q$, for NiTiFe SMAs. Note that the flow stress data corresponding to $\varepsilon = 0.5$ have been taken.

The activation energy for hot working, $Q$, which is an important physical parameter indicating the plastic deformability of the alloy, can be estimated the following equation that is obtained by differentiating Eq [12].

$$(16) Q=R\left\{\frac{\partial \ln \dot{\varepsilon}}{\partial \ln[\sinh(\alpha\sigma)]}\right\}_T\left\{\frac{\partial \ln[\sinh(\alpha\sigma)]}{\partial \frac{1}{T}}\right\}_{\dot{\varepsilon}}$$

$$(17) Q=RQ_1Q_2$$

The first term on the right hand side of Eq. [16], $\{\frac{\partial \ln \dot{\varepsilon}}{\partial \ln[\sinh(\alpha\sigma)]}\}$, $Q_1$, refers to the slope of $\ln \dot{\varepsilon}$ vs. ln [sinh(ασ)] at different $T$ and the second term $\{\frac{\partial \ln[\sinh(\alpha\sigma)]}{\partial \frac{1}{T}}\}$, $Q_2$, refers to slope of ln [sinh(ασ)] vs. the reciprocal of $T$ at various $\dot{\varepsilon}$. In order to calculate $Q$ for the SMAs, the estimated values of $\alpha$ at $\varepsilon$ = 0.5 were used. The $\ln \dot{\varepsilon}$ vs. ln [sinh(ασ)] data at different $T$ as well as the ln [sinh(ασ)] vs. $1/T$ data at different $\dot{\varepsilon}$ are plotted to estimate $Q_1$ and $Q_2$. See representative plots for NiTiFe SMA in Fig. 5(c) and (d), respectively The average values of the slopes ($Q_1$ and $Q_2$) are then substituted in Eq [17]. to calculate $Q$. The apparent $Q$ values obtained at a $\varepsilon$ = 0.5 for NiTi, NiTiCu and NiTiFe SMAs are 173.4, 188.9 and 187.1 kJ/mol, respectively, in the B2 austenite phase. The obtained values of $Q$ are compared with the reported values in the literature. Oppenheimer et al. [64] reported a $Q$ value of 155 kJ/mol for $Ni_{49.8}Ti_{50.2}$, which is approximately equal to activation energy for diffusion of Ni in NiTi. Dehghani and Khamei [33] obtained a $Q$ value of 251 kJ/mol in Ni rich $Ni_{55}Ti_{45}$ SMA. The obtained value of $Q$ for NiTi in the present study (173.4 kJ/mol) is in between these two values. Jiang et al. [65] and Shujuan et al. [47] reported $Q$ values of 198 and 200.4 kJ/mol for $Ni_{45}Ti_{50}Cu_5$ and $Ni_{47}Ti_{50}Fe_3$, respectively. The values of $Q$ for NiTiCu (188.9 kJ/mol) and NiTiFe (187.1 kJ/mol) match well with these. The marginal differences could be due to differences in the starting grain size and/or deviations in the compositions of the SMAs.

Values of $Q$ at $\varepsilon$ = 0.1, 0.2, 0.3 and 0.4 were also estimated for the SMAs using similar procedure. The variation of $Q$ with $\varepsilon$ is plotted in Fig. 6. As seen, $Q$ ranges between 150 and 190 kJ/mol. It first decreases when $\varepsilon$ is increased from 0.1 to 0.2 for NiTi and NiTiFe SMAs and increases linearly thereafter for all the three SMAs. $Q$ for NiTiCu and NiTiFe are higher than that of NiTi for $\varepsilon \geq 0.2$. Therefore, the apparent $Q$ for deformation increases with Cu and Fe addition in binary NiTi SMA, i.e., deformation resistance of the binary NiTi SMA increases with Cu and Fe addition.

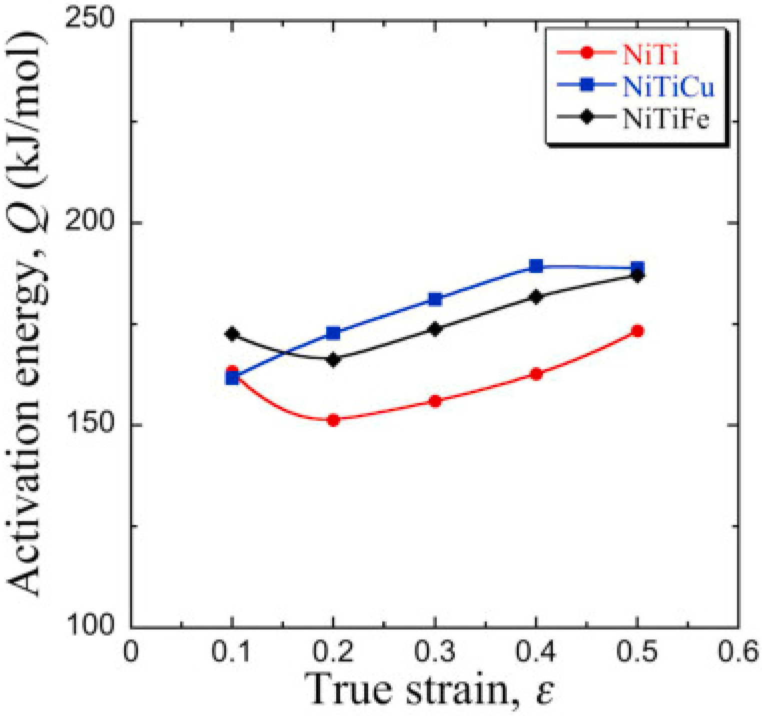


1. Download: Download high-res image (256KB)
2. Download: Download full-size image

Fig. 6. Variation of activation energy for deformation, $Q$, with $\varepsilon$ in NiTi, NiTiCu and NiTiFe SMAs.

### 4.4.2. Constitutive equations as a function of Zener-Hollomon parameter

The materials constants obtained in section 4.4.1 are used to model the deformation behavior of the SMAs using the constitutive equations. One of these equations is temperature compensated strain rate parameter, i.e. the Zener-Hollomon parameter, $Z$:

$$(18) Z = \dot{\varepsilon} \exp = [\frac{Q}{RT}] = A[\sinh(\alpha\sigma)]^{n},$$

which can be transformed into:

$$(19) \sigma = \frac{1}{\alpha} \ln\{(\frac{Z}{A})^{\frac{1}{n}} + \sqrt{(\frac{Z}{A})^{\frac{2}{n}} + 1}(ZA)2/n+1\}$$

On the basis of apparent activation energy, $Z$ can be used to characterize combined effect of $T$ and $\dot{\varepsilon}$ on the deformation process, especially deformation resistivity. Taking the natural logarithm on both sides of Eq [18]. gives:

$$(20) \text{In}Z = \text{In}A + n[\sinh(\alpha\sigma)]$$

Substituting $Q$ and different values of $T$ and $\dot{\varepsilon}$ into Eq. [18], values of $Z$ and $\ln Z$ are estimated for NiTi, NiTiCu and NiTiFe. The plot of $\ln Z$ vs. $\ln[\sinh(\alpha\sigma)]$ displayed in Fig. 7 confirms Eq [20]. and implies that a single deformation mechanism is dominant in the investigated $T$- $\dot{\varepsilon}$ range. At any given value of ln[sinh($\alpha\sigma$)], ln Z for NiTiCu was higher than those of NiTiFe and NiTi SMAs. Good linear correlation obtained between ln $Z$ vs. ln[sinh($\alpha\sigma$)] exist. This also confirms constitutive equations of the SMAs can be represented by hyperbolic sine function. The slopes of the plots give values of ln $A$ and $n$ and are summarized in the inset of Fig. 7.

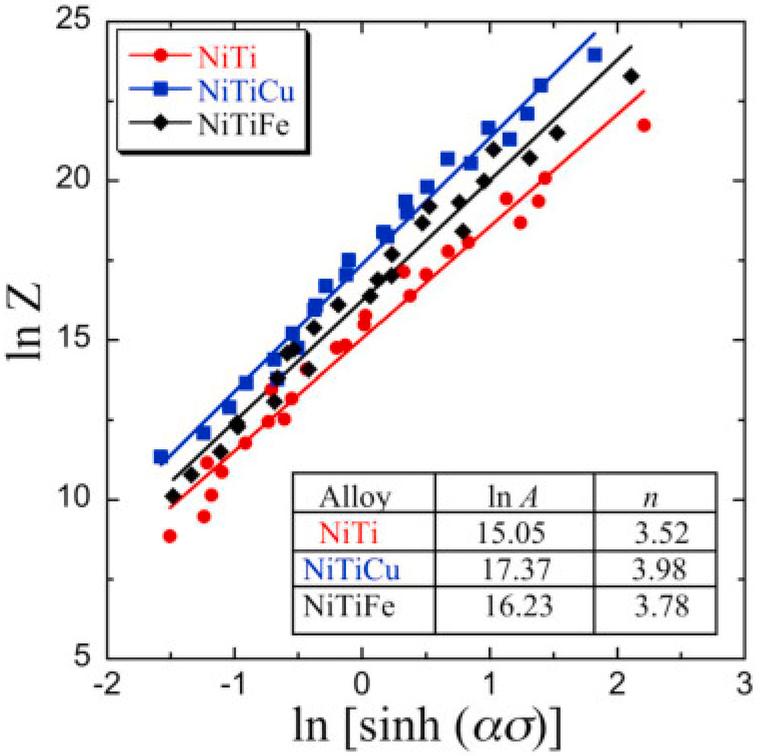


1. Download: Download high-res image (357KB)
2. Download: Download full-size image

Fig. 7. Plot of the hyperbolic sine function of stress (at $\varepsilon$ = 0.5) vs. the Zener-Hollomon parameter, Z.

On the basis of above analysis, constitutive equations that describe the flow stress of NiTi, NiTiCu and NiTiFe as a function of $\dot{\varepsilon}$ and deformation $T$ at $\varepsilon$ = 0.5 can be written as:

$$\text{NiTi: (21.a) } \dot{\varepsilon} = 3.43\times10^{6}[\sinh(0.009\sigma)]^{3.52}\exp[\frac{-173.4\times10^{3}}{RT}]$$

$$\text{NiTiCu: (21.b) } \dot{\varepsilon} = 34.9\times10^{6}[\sinh(0.006\sigma)]^{3.98}\exp[\frac{-188.9\times10^{3}}{RT}]]$$

$$\text{NiTiFe: (21.c) } \dot{\varepsilon} = 11.16\times10^{6}[\sinh(0.009\sigma)]^{3.78}\exp[\frac{-187.1\times10^{3}}{RT}]]$$

On the basis of the above and the material constants $A$, α, $n$ obtained, the flow stress of the SMAs at $\varepsilon$ = 0.5 can be rewritten in terms of $Z$ as:

$$\text{NiTi: (22.a)}\ \sigma=\frac{1}{0.009}\ln\{(\frac{Z}{3.43\times10^{6}})^{\frac{1}{3.52}}+\sqrt{(\frac{Z}{3.43\times10^{6}})^{\frac{2}{3.52}}+1}\}$$

$$\text{(22.b)}\ \sigma=\frac{1}{0.006}\ln\{(\frac{Z}{3.49\times10^{7}})^{\frac{1}{3.98}}+\sqrt{(\frac{Z}{3.49\times10^{7}})^{\frac{2}{3.98}}+1}\}$$

$$\text{NiTiFe: (22.c)}\ \sigma=\frac{1}{0.009}\ln\{(\frac{Z}{1.11\times10^{7}})^{\frac{1}{3.78}}+\sqrt{(\frac{Z}{1.11\times10^{7}})^{\frac{2}{3.78}}+1}\}$$

### 4.4.3. Verification of constitutive equations

The constitutive equations derived in Eq [22]. for the SMAs can be used as inputs for simulating the material forming processes under specific deformation conditions. It also allows direct calculation of flow stress required during deformation based on the process parameters ($T$ and $\dot{\varepsilon}$). In order to verify the accuracy of the constitutive equations, a comparison between the flow stress values determined experimentally and those predicted from the constitutive equations (Eq [22]) was carried out [34,66]. Fig. 8 compares the experimental flow stress of the SMAs at $\varepsilon$ = 0.5 with the flow stress derived from the constitutive equations. A good agreement between the experimental and predicted values was obtained in Fig. 8 with correlation coefficient of $R^2$~ 0.98. The accuracy of the constitutive equations was also quantified using standard statistical parameters like average absolute relative error (AARE) [66]. The AARE is expressed as:

$$\text{(23) AARE(\%)}=\frac{1}{N}\sum_{i=1}^{N}\left|\frac{E_i-P_i}{E_i}\right|\times100$$

where $E_i$ and $P_i$ are the experimental and predicted flow stress values and $N$ is the number of data points. The calculated values of AARE for NiTi, NiTiCu and NiTiFe are 9.73, 19 and 10.7% respectively. Based on the values of $R^2$ and AARE, it can be confirmed that Arrhenius type constitutive equation developed for NiTi, NiTiCu and NiTiFe in the $T$ range of 800–1050 °C and $\dot{\varepsilon}$ = $10^{-3}$ to $10^{+1}$ $s^{-1}$ can successfully predict flow stress of the alloys. The observed discrepancy between measured and predicted flow stress values could be related to variation in the grain size or localized formation of stress induced martensite during deformation as the Arrhenius type constitutive equation is valid only when the material parameters like the phase fraction, grain size remain constant and do not change with the temperature.

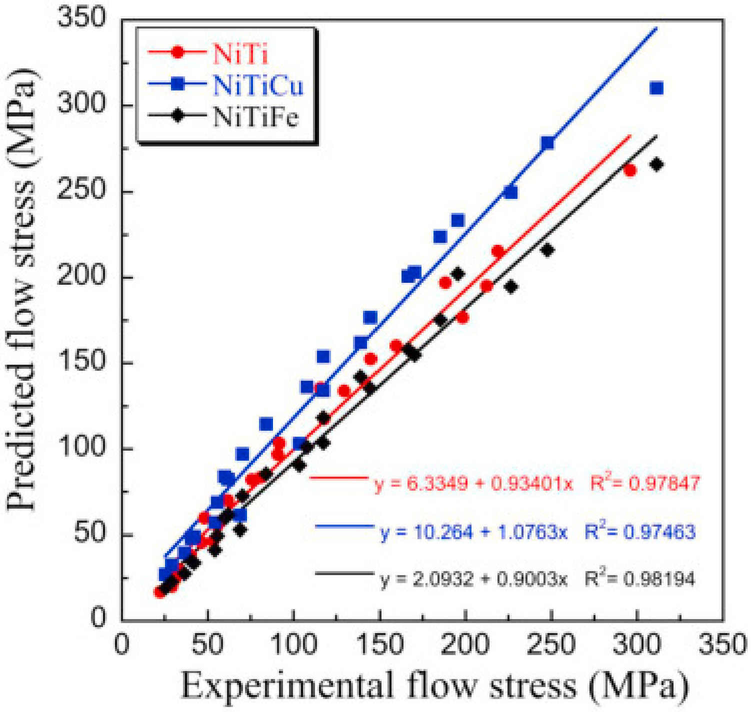


1. Download: Download high-res image (387KB)
2. Download: Download full-size image

Fig. 8. Comparison between experimental flow stress data (at $\varepsilon = 0.5$) with predicted flow stress data in the plastic regime based on derived constitutive equations.

## 4.5. Processing maps

Processing and strain-rate sensitivity maps of NiTi, NiTiCu and NiTiFe generated for $\varepsilon = 0.5$ and are shown in Fig. 9, Fig. 10, respectively. Instability regimes with $\zeta < 0$ are shaded grey in the processing maps in Fig. 9. The numbers on the contour lines represent $\eta$ (%) and $m$ values, respectively. These maps show peaks in $\eta$ and $m$, projected onto the 2-D space, which signify different deformation mechanism operating at different combinations of $T$ and $\dot{\varepsilon}$. A domain in these maps is defined as the window in the $T$ and $\dot{\varepsilon}$ space, over which a change in the values of $\eta$, $m$ and $\zeta(\dot{\varepsilon})$ are significant. These domains represent specific microstructural features and deformation mechanism that contribute to power dissipation. A summary of the informations extracted from the maps are summarized in Table 2. It lists various domains that operate in various $T$ and $\varepsilon^{\cdot}$ regimes, corresponding $\eta$, $m$ and $\zeta$ values, key microstructural features observed via microscopy and the likely deformation mechanism(s). Based on Table 2 and Fig. 9, Fig. 10, processing maps of NiTi, NiTiCu and NiTiFe SMAs can be broadly classified into 3 stable domains ($\zeta > 0$) for hot working, which are illustrated as Domain-1, Domain-2 and Domain-3 in Fig. 9.

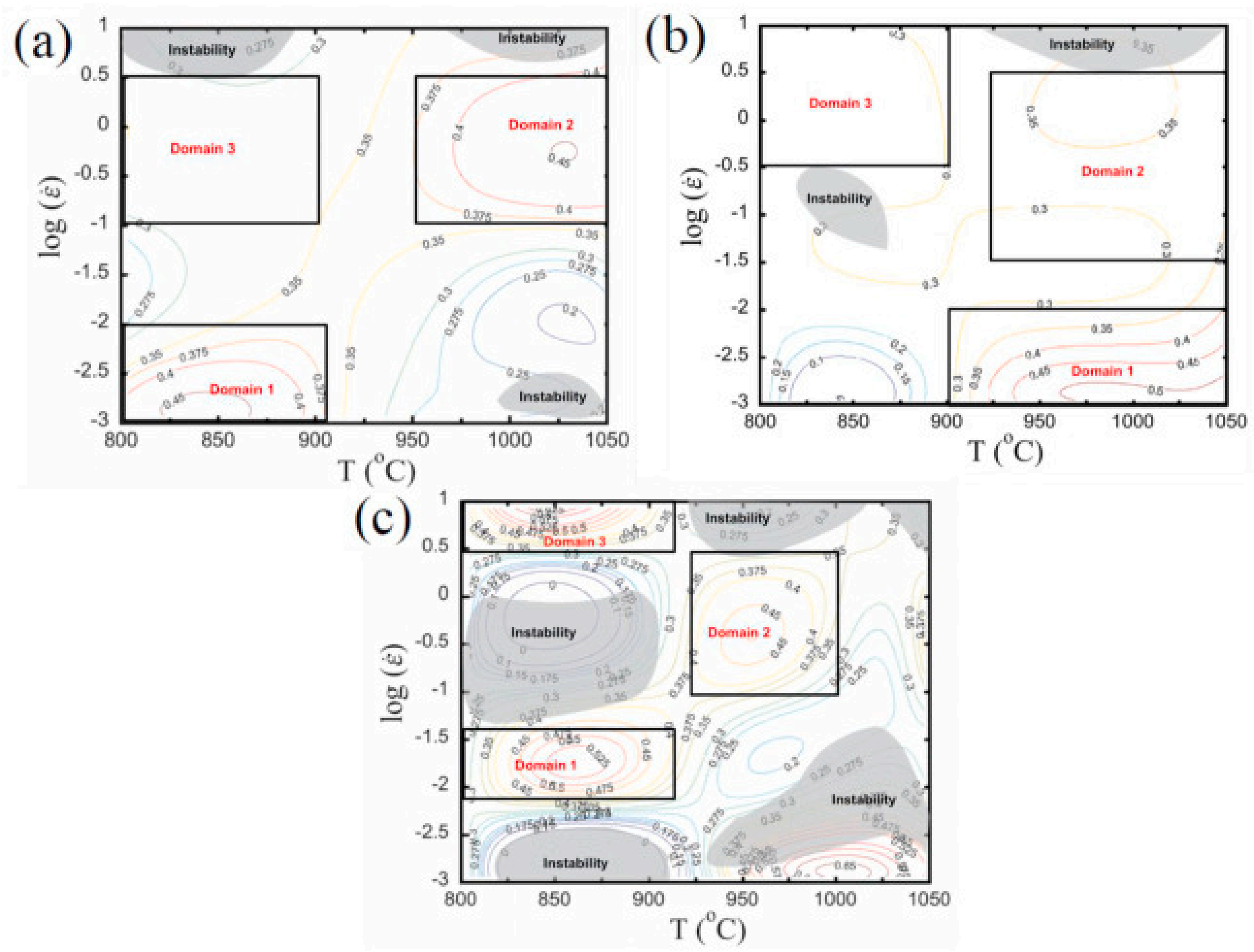


1. Download: Download high-res image (652KB)
2. Download: Download full-size image

Fig. 9. Processing maps of (a) NiTi, (b) NiTiCu and (c) NiTiFe SMAs generated at $\varepsilon$ = 0.5. Instability regions are shown as shaded grey.

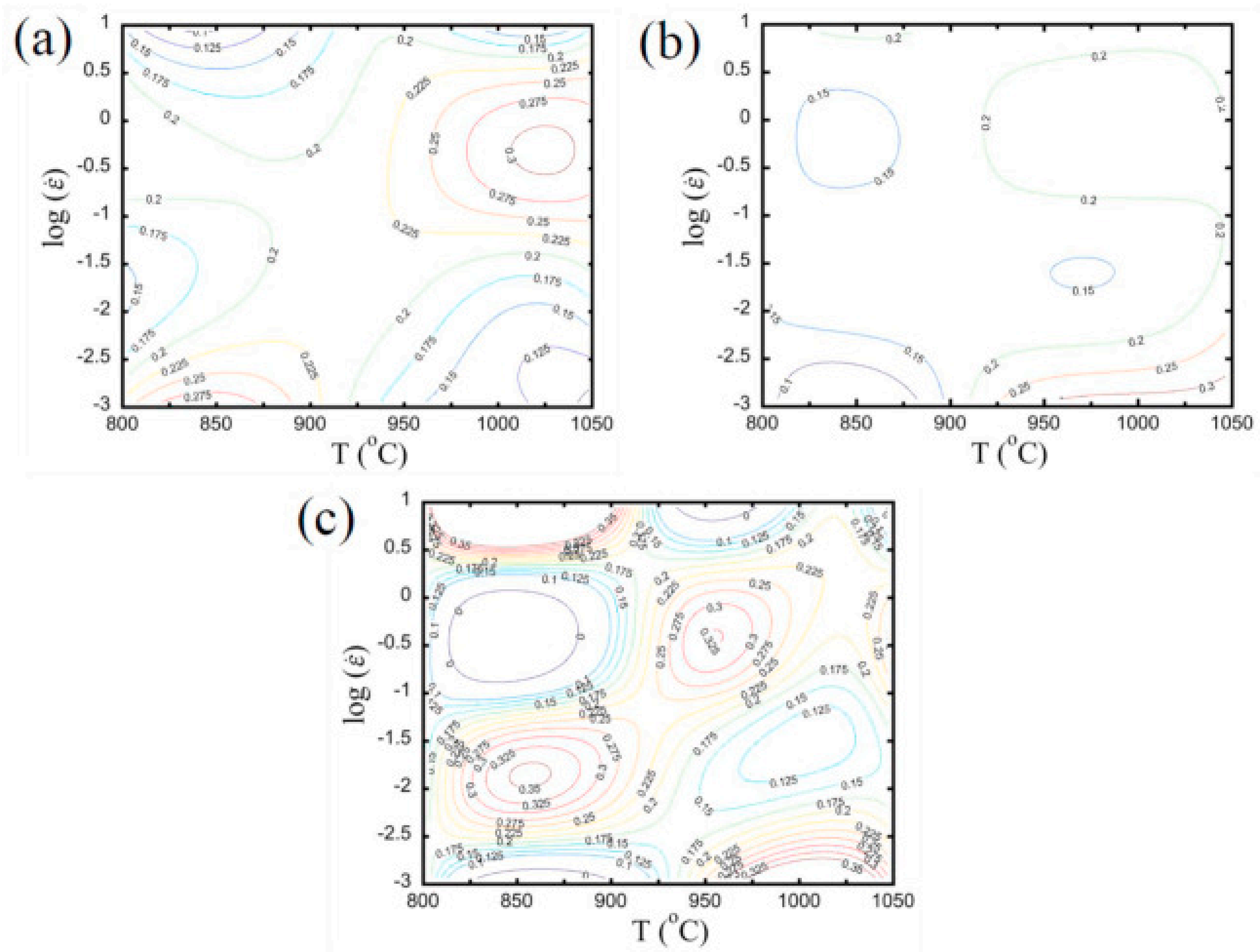


1. Download: Download high-res image (623KB)
2. Download: Download full-size image

Fig. 10. Strain rate sensitivity maps of (a) NiTi, (b) NiTiCu and (c) NiTiFe SMAs generated at $\varepsilon = 0.5$.

Table 2. List of domains within the processing window of $T = 800–1050$ °C and $\dot{\varepsilon} = 10^{-3}$ to $10^{+1}$ s$^{-1}$. Values of $\eta$, $m$, $\zeta$, key microstructural features observed and the likely deformation mechanism(s) operating in various domains are also provided.

| Alloy | Domain | T (°C) | $\dot{\varepsilon}$ (s$^{-1}$) | $\eta$ (%) | *m* | $\zeta$ | Key microstructural feature/deformation mechanism |
|---|---|---|---|---|---|---|---|
| NiTi | 1 | 800–910 | $10^{-3}$ – $10^{-2}$ | 28–45 | 0.18–0.275 | Positive | Elongated & serrated grains/DRV (dominating), partial DRX |
| | 2 | 950–1050 | $10^{-1}$ – $10^{+0.5}$ | 37.5–45 | 0.22–0.30 | Positive | Equiaxed grains/DRX |
| | 3 | 800–900 | $10^{-1}$ – $10^{+0.5}$ | 30–35 | 0.175–0.20 | Positive | Elongated grains/DRV (dominating), partial DRX |
| NiTiCu | 1 | 900–1050 | $10^{-3}$ – $10^{-2}$ | 30–50 | 0.20–0.30 | Positive | Elongated grains/partial DRX, DRV (dominating) |

| Alloy | Domain | T (°C) | $\dot{\varepsilon}$ ($s^{-1}$) | $\eta$ (%) | *m* | $\zeta$ | Key microstructural feature/deformation mechanism |
|---|---|---|---|---|---|---|---|
| | 2 | 925–1050 | $10^{-1.5}$ – $10^{+0.5}$ | 30–35 | 0.15–0.20 | Positive | |
| | 3 | 800–900 | $10^{-0.5}$ – $10^{+1}$ | 30 | 0.15–0.20 | Positive | |
| NiTiFe | 1 | 800–910 | $10^{-2.1}$ – $10^{-1.4}$ | 30–52.5 | 0.18–0.35 | Positive | Equiaxed grains with few unrecrystallized grains/partial DRX, DRV (dominating) |
| | 2 | 925–1000 | $10^{-1}$ – $10^{+0.5}$ | 35–45 | 0.20–0.32 | Positive | Equiaxed grains/DRX (dominating) |
| | 3 | 800–920 | $10^{+0.5}$– $10^{+1}$ | 35–62.5 | 0.25–0.35 | Positive | Flow localization |

The workability of the material cannot be judged from the processing map alone. In order to validate the processing maps and to determine the operating deformation mechanism(s) in various domains, deformed specimens are analyzed metallographically and corroborated through power dissipation values. It is important to mention that the microstructures of the SMAs deformed in the B2 austenite phase (800–1050 °C) undergo phase transformation during cooling. The microstructures exactly after hot deformation are unable to be retained at room temperature. Therefore, the deformed microstructures presented are of B19' martensite phase. Various domains and its microstructural features are discussed below.

## Domain-1

For NiTi, Domain-1 occurs at $T$ = 800–910 °C, $\dot{\varepsilon}$ = $10^{-3}$ to $10^{-2}$ $s^{-1}$ with $\eta$ = 28–45%. The maximum in deformation efficiency of $\eta$ = 45% occurs at $T$ = 840 °C and $\dot{\varepsilon}$ = $10^{-3}$ $s^{-1}$. The addition of Cu in NiTi SMA extends Domain-1 to higher $T$ (900–1050 °C) at the same $\dot{\varepsilon}$ range but with higher $\eta$ values (30–50%), with a maximum deformation efficiency of $\eta$ = 50% at $T$ = 1000 °C and $\dot{\varepsilon}$ = $10^{-3}$ $s^{-1}$. The addition of Fe shrinks Domain-1 and shifts it to higher $\dot{\varepsilon}$ = $10^{-2.1}$ to $10^{-1.4}$ $s^{-1}$ at same $T$ (800–910 °C) with $\eta$ = 30–52.5%. Despite $\zeta > 0$, Domain-1 in NiTiFe should be avoided during processing, as it lies intermediate between two instability regimes (Fig. 9c). Microstructures of the specimens deformed in Domain-1 are illustrated in Fig. 11(a)–(c). The pancake type of grain morphology still persists in both NiTi and NiTiCu when deformed in Domain-1. The microstructure of NiTi SMA also revealed limited serrations at the grain boundaries (broken arrow in Fig. 11a), this indicates to occurrence of DRV [35,36]. The formation of serrated grain boundaries in NiTi could be related to the local migration of grain boundaries in response to boundary tension of sub-grains and local variation in the dislocation density [67]. Few dynamically recrystallized grains are also observed near grain boundaries, which are shown with solid arrows in Fig. 11a. The microstructure of NiTiCu showed limited DRX (solid arrows in Fig. 11b) with the alignment of grains along the direction of the flow (Fig. 11b). The microstructure of NiTiFe appears to be more of equiaxed with few non-recrystallized grains (Fig. 11c). Another interesting observation was the formation of long and lenticular type twin structures inside the martensite grains of NiTi, which were otherwise difficult to resolve in NiTiCu and NiTiFe.

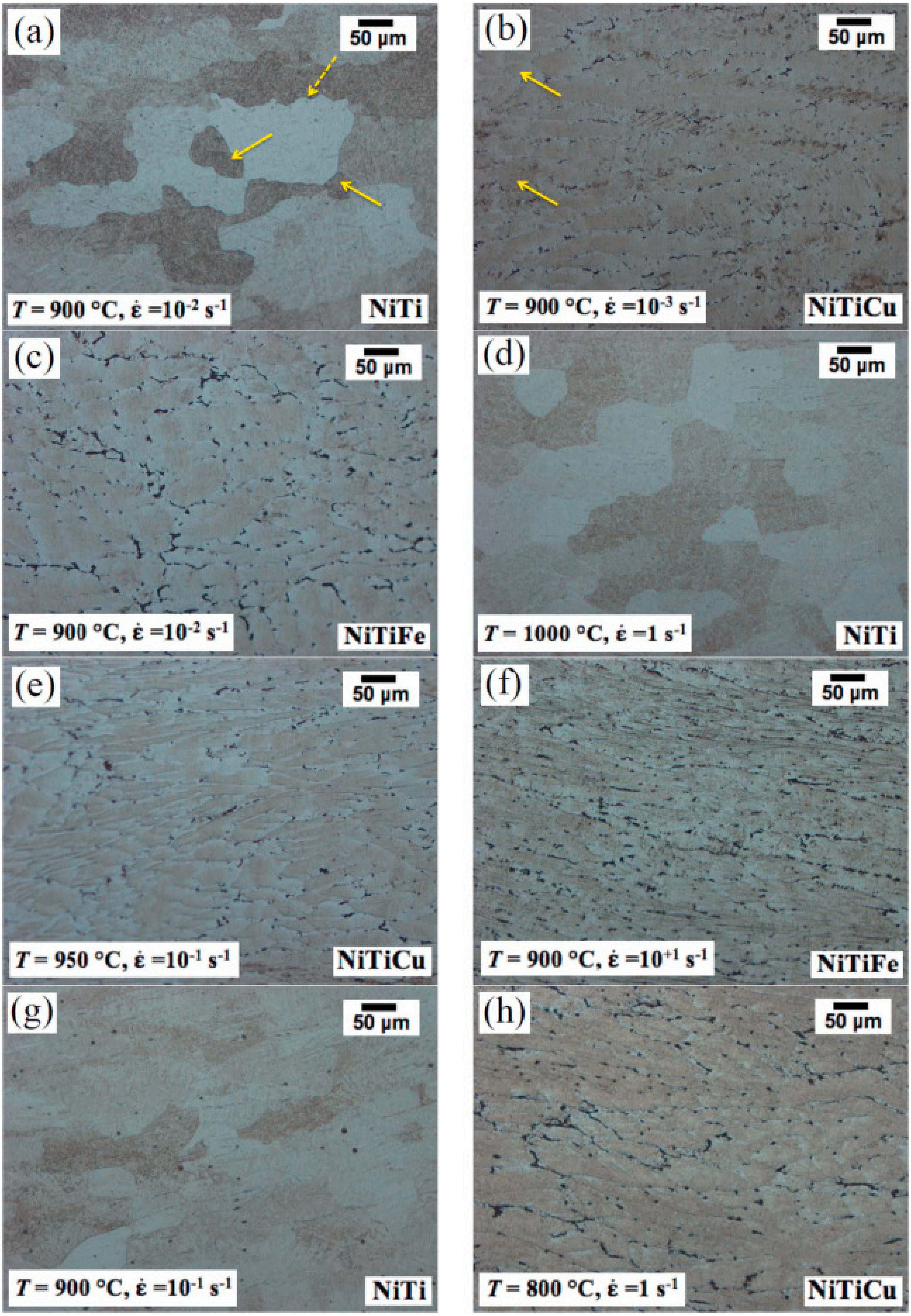

(a)
50 μm
T = 900 °C, ε̇ =10^-2 s^-1
NiTi
(b)
50 μm
T = 900 °C, ε̇ =10^-3 s^-1
NiTiCu
(c)
50 μm
T = 900 °C, ε̇ =10^-2 s^-1
NiTiFe
(d)
50 μm
T = 1000 °C, ε̇ =1 s^-1
NiTi
(e)
50 μm
T = 950 °C, ε̇ =10^-1 s^-1
NiTiCu
(f)
50 μm
T = 900 °C, ε̇ =10^+1 s^-1
NiTiFe
(g)
50 μm
T = 900 °C, ε̇ =10^-1 s^-1
NiTi
(h)
50 μm
T = 800 °C, ε̇ =1 s^-1
NiTiCu

1. Download: Download high-res image (2MB)
2. Download: Download full-size image

Fig. 11. Optical micrographs of NiTi, NiTiCu and NiTiFe SMAs deformed at different temperatures and strain rates. Compression axis is vertical. DRX grains in (a) and (b) are shown with solid arrows and DRV in (a) with broken arrow.

Both DRV and DRX are the predominant softening mechanisms operating during hot working of the alloys. The DRV process involves dislocation climb, cross-slip, and glide of dislocations which results in the formation of sub-grains with low misorientation [67]. Here, the softening mechanism is related to annihilation of dislocations of opposite sign. On the other hand in DRX, nucleation and growth of new grains occurs at the heavily deformed regions such as grain boundaries and deformation bands [67]. At a fixed deformation degree, $\dot{\varepsilon}$ and $T$ (or $Z$) have an important influence on the occurrence of DRV and DRX [67]. The microstructure developed after hot working depends upon both $\varepsilon$ and Z [67]. The $\eta$ and $m$ values associated with DRV and DRX generally range between $\eta$ = 20–30%, $m$ < 0.20 and $\eta$ = 35–50%, $m$ > 0.30 respectively [48]. The obtained values of $\eta$ and $m$ for the SMAs investigated in this work are within this range, see Table 2, indicating both DRV and DRX are operating in Domain-1. However, microstructural analyses of the deformed alloys indicate only partial DRX with DRV dominating in Domain-1. The low strain rates and intermediate temperatures (low Z values) in this domain also promote DRV over DRX. Therefore, the applied level of strain $\varepsilon$ = 0.7, $T$ and $\dot{\varepsilon}$ range operating in this domain are not sufficient for complete DRX.

## Domain-2

The Domain-2 in NiTi, NiTiCu and NiTiFe are located at high $T$ and $\dot{\varepsilon}$ with intermediate to high $\eta$ values. For NiTi, it occurs at $T$ = 950–1050 °C, $\dot{\varepsilon} = 10^{-1}$ to $10^{+0.5}$ $s^{-1}$ with widely spaced contours of $\eta$ = 38–45% (Fig. 9a). The peak in deformation efficiency of $\eta$ = 45% occurs at $T$ = 1020 °C and $\dot{\varepsilon} = 10^{-0.3}$ $s^{-1}$. Domain-2 in NiTiCu is much wider ($T$ = 925–1050 °C and $\dot{\varepsilon} = 10^{-1.5}$ to $10^{+0.5}$ $s^{-1}$) in comparison to NiTi but with lower $\eta$ values (30–35%). In NiTiFe, it shifts to lower $T$ range (925–1000 °C) at same $\dot{\varepsilon}$ with $\eta$ values (35–45%) comparable to NiTi. The maximum $\eta$ of 45% in NiTiFe occurred at $T$ = 960 °C and $\dot{\varepsilon} = 10^{-0.5}$ $s^{-1}$. The microstructures of the SMAs deformed in Domain-2 are illustrated in Fig. 11(d) and (e). Increasing the deformation temperature and strain rate in Domain-2 resulted in complete DRX of the grains in NiTi and NiTiFe (Fig. 11d). This is also confirmed from the $\eta$ and $m$ values of around 35–45% and 0.20–0.32 for NiTi and NiTiFe in Domain-2, which is within the range of occurrence of DRX [48]. The pancake type of grain morphology observed in Domain-1 (Fig. 11a) for NiTi is completely broken in Domain-2 with the formation of equiaxed grains with an average grain size of ~70 µm. In general, a high value of $\eta$ indicates good hot workability of the material with higher proportion of the input power used for microstructure reconstitution through DRX process. DRX also provides stable flow stress during processing and is a chosen “safe” domain for optimizing hot workability during bulk metal working [48].

A comparison of the microstructures of NiTiCu deformed in Domain-1 and Domain-2 reveals similar microstructural features with limited or no DRX (Fig. 11e). Moreover, the $T$ range for Domain-1 and Domain-2 are similar (~900–1050 °C), while increasing $\dot{\varepsilon}$ from Domain-1 to Domain-2 does not lead to an increased fraction of the DRX grains. The $\eta$ and $m$ values are around 30–35% and 0.15–0.20 in Domain-2 (see Table 2), which is lower than that are typical of DRX. This suggests DRV as the operating deformation mechanism in NiTiCu in Domain-2.

## Domain-3

Domain-3 occurs at low $T$ and high $\varepsilon^{\cdot}$ range with low to high $\eta$ values. In NiTi, it occurs at $T$ = 800–900 °C and $\dot{\varepsilon}$ = $10^{-1}$ to $10^{+0.5}$ $s^{-1}$ with widely spaced $\eta$ contours with values 30–35%. In NiTiCu, it occurs in the same $T$ range but at a higher $\dot{\varepsilon}$ range ($10^{-0.5}$ to $10^{+1}$ $s^{-1}$) with low $\eta$ value (30%). Fe addition in NiTi shifts it to further higher $\dot{\varepsilon}$ ($10^{+0.5}$ to $10^{+1}$ $s^{-1}$) at similar $T$ range (800–920 °C). It is important to note that contour lines of $\eta$ are very narrowly spaced with large variation in the $\eta$ values from 35 to 62.5% (Fig. 9c) indicating a steeply graded domain [68]. Such high efficiency of $\eta$ contours increases with increasing $\dot{\varepsilon}$ and decreasing $T$ (Fig. 9c). This typically denotes the occurrence of microstructural instability during deformation through flow localization, void formation, and cracking [48]. The microstructural analysis performed in Domain-3 for NiTiFe deformed at $T$ = 900 °C and $\dot{\varepsilon}$ = 10 $s^{-1}$ revealed extensive flow localization (Fig. 11f), even though this deformation condition is located in the stable domain of the processing map. Fig. 11(g) and (h) show the corresponding deformed micrographs of NiTi and NiTiCu. The former reveals few DRX grains with extensive twinning within the grains. The microstructural features of NiTiCu are similar to those in Domain-1 and Domain-2 with limited DRX, and DRV as the operating deformation mechanism. The low values of $\eta$ and $m$ in Domain-3 is another reason for the occurrence of DRV in NiTi and NiTiCu. Overall, based on the microstructural analysis, low values of $\eta$ and $m$, and its proximity to the instability regions, Domain-3 is not an ideal regime for hot working of the SMAs and should be avoided during processing.

## 4.5.1. Instability regions

The flow instability criterion defined in Eq [11]. identified following regions (shaded grey in Fig. 9) where it might occur during processing. NiTi: $T$ = 800–1050 °C & $\dot{\varepsilon}$ >$10^{-1}$ to $10^{+0.5}$ $s^{-1}$ and $T$ = 1000–1050 °C & $\dot{\varepsilon}$ = $10^{-3}$ to $10^{-2.5}$ $s^{-1}$; NiTiCu: $T$ = 820–860 °C & $\dot{\varepsilon}$ = $10^{-1.5}$ to $10^{-0.5}$ $s^{-1}$ and $T$ = 925–1050 °C & $\dot{\varepsilon}$ > $10^{+0.5}$ $s^{-1}$; NiTiFe: $T$ = 820–1050 °C & $\dot{\varepsilon}$ = $10^{-3}$ to $10^{-2}$ $s^{-1}$, $T$ = 925–1050 °C & $\dot{\varepsilon}$ > $10^{+0.5}$ $s^{-1}$, and $T$ = 800–900 °C & $\dot{\varepsilon}$ = $10^{-1.5}$ to $10^{+0}$ $s^{-1}$. As seen from Fig. 9, the addition of Fe to NiTi significantly expanded the flow instability regions whereas Cu showed no effect. Representative micrographs of the samples deformed in the instability regions are displayed in Fig. 12. The microstructure of NiTiCu deformed at $T$ = 950 °C and $\dot{\varepsilon}$ = $10^{+1}$ $s^{-1}$ showed microstructure instability in the form of flow localization (Fig. 12a). The microstructures of the SMAs deformed in other unstable domains also revealed instability in the form of flow localization with varying intensities, see Fig. 12(b) and (c). Flow lines formed within the flow localization zone are long and straight in nature and on few occasions curvy also. This is consistent with the findings of Morakabati et al. [35,36] where they have shown flow localization as one of the instability mechanism during hot working of $Ni_{49.8}Ti_{50.2}$ SMA at intermediate to high strain rates. In the present work, no other microstructural instabilities in the form of cracking or void formation unlike as observed by Morakabati et al. was detected in the examined $T$- $\dot{\varepsilon}$ range. Clearly, in the unstable domains slip dominated plastic flow is limited.

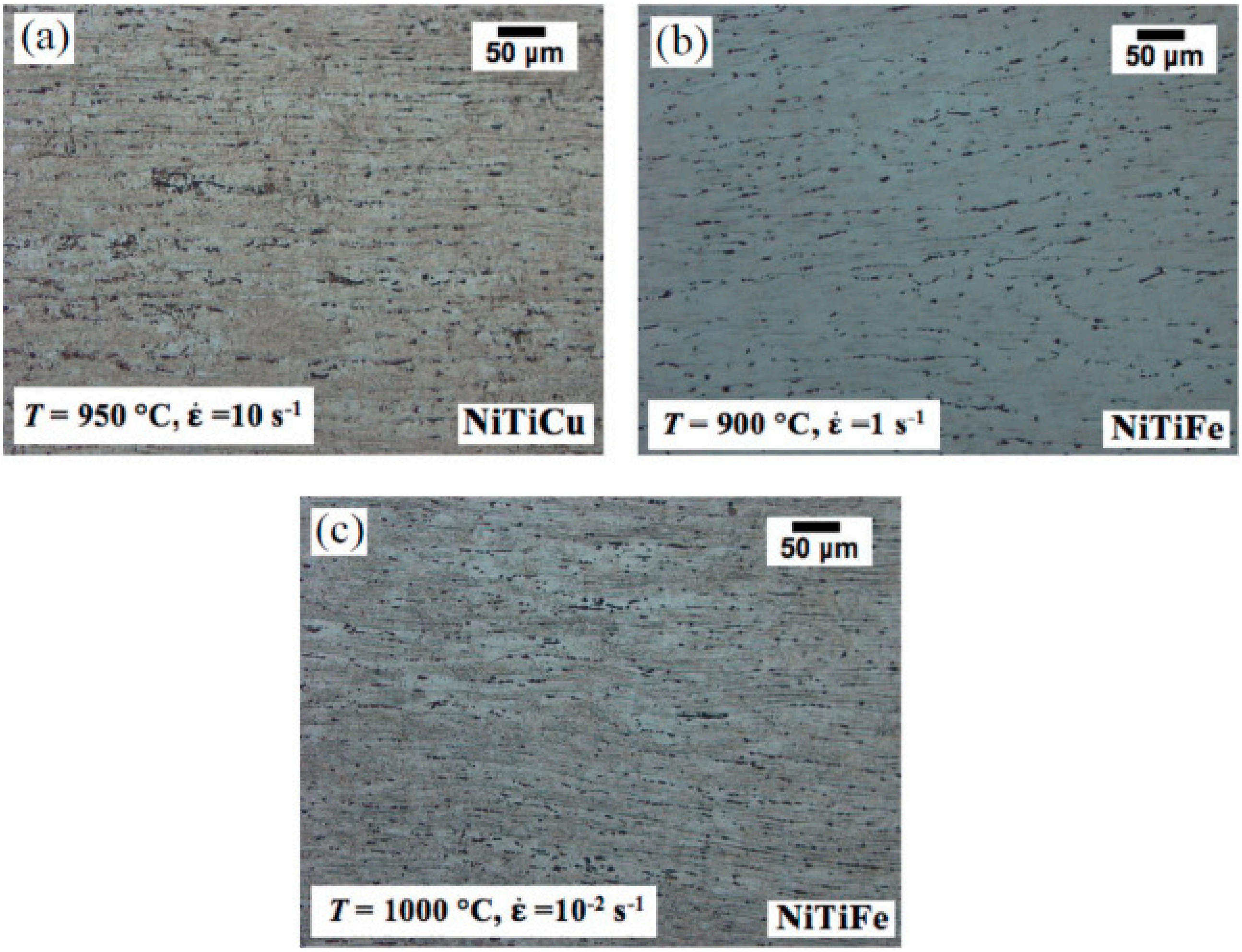


Download: Download high-res image (1MB)
Download: Download full-size image

Fig. 12. Optical micrographs of the SMAs deformed in the unstable domains showing flow localization. (a) NiTiCu deformed at $T$ = 950 °C, $\dot{\varepsilon}$ = 10 $s^{-1}$. NiTiFe deformed at (b) $T$ = 900 °C, $\dot{\varepsilon}$ = 1 $s^{-1}$ and (c) $T$ = 1000 °C, $\dot{\varepsilon}$ = $10^{-2}$ $s^{-1}$. Compression axis is vertical.

To summarize, addition of Cu in NiTi SMA enlarges stable deformation regime for hot working, whereas Fe addition shrinks it. Although Cu extends stable hot working zones but the extent of applied strain $\varepsilon = 0.7$ is not sufficient to obtain complete DRX microstructure. This is also evident from high values of $Z$ and $Q$ in NiTiCu in comparison with NiTi and NiTiFe (Fig. 6, Fig. 7). Domain-2 at high $T$ and intermediate $\dot{\varepsilon}$ appears to be safe domain for hot working for NiTi, NiTiCu and NiTiFe. The $\eta$ values in Domain-2 for the SMAs vary between 30 and 45%.

## 4.6. Critical stress for the onset of dynamic recrystallization

As mentioned earlier in section 4.5, DRX in NiTiCu is limited in comparison to NiTi and NiTiFe SMAs. The sluggish nature of DRX kinetics in NiTiCu in Domain-2 is analyzed further by direct comparison of the critical stress, $\sigma_c$, required for the onset of DRX with NiTi and NiTiFe. While the peak stress observed in the flow curves in Domain-2 is indicative of the occurrence of DRX, the onset of DRX cannot be identified from it alone [69]. In general, DRX initiates before the peak in the $\sigma$-$\varepsilon$ response. In view of this, a simplified model proposed by Najafizadeh and Jonas [69] for predicting the onset of DRX in Domain-2 was employed here. In this model, the $\sigma_c$ for the onset of DRX is determined from the inflection point on the strain-hardening rate ($\theta = \mathrm{d}\sigma\mathrm{d}\varepsilon$) versus flow stress curve before the peak stress is reached [[69], [70], [71]]. In some problematic cases where inflection point is not clearly defined in the $\theta$ vs. $\sigma$ curves, $\sigma_c$ is determined from the minimum in the plot of - $\mathrm{d}\theta\mathrm{d}\sigma$ vs. $\sigma$. A similar approach has been used by Mirzadeh and Parsa [39] to study the occurrence of DRX during hot deformation of $Ni_{50.5}Ti_{49.5}$. It is important to note that the inflection in $\theta$ vs. $\sigma$ or minimum in $-\frac{\mathrm{d}\theta}{\mathrm{d}\sigma}$ vs. $\sigma$ is not expected when deformation is dominated by DRV process [71].

Values of $\sigma_c$ got for NiTi, NiTiCu and NiTiFe SMAs are plotted against the operating $T$-$\dot{\varepsilon}$ range for Domain-2 in Fig. 13. Here closed and open symbols refers to data at $\dot{\varepsilon} = 10^{-1}$ and 1 $s^{-1}$, respectively. It is seen that $\sigma_c$ decreases steadily with increasing $T$ and decreasing $\dot{\varepsilon}$. Since the driving force for the nucleation of DRX grains increases with increasing $T$, the critical stress/strain required for the onset of DRX decreases [67]. It appears that the addition of Cu to NiTi increases $\sigma_c$ while Fe decreases it. Representative $\theta$ vs. $\sigma$ and $-\frac{\mathrm{d}\theta}{\mathrm{d}\sigma}$ vs. $\sigma$ plots for the SMAs at $T = 1000$ °C and $\dot{\varepsilon} = 1$ $s^{-1}$ are compared in Fig. 14(a) and (b). Based on Fig. 14 and analysis made from other deformation conditions in Domain-2, following observations can be made: $\theta$ decreases steadily with increasing flow stress probably due to onset of DRX. A change in the slope of $\theta$ vs. $\sigma$ plots at the inflection point representing $\sigma_c$ was observed (marked by arrows in Fig. 14a). Afterwards, the curves intersect $\theta = 0$ at the peak stress. The $\sigma_c$ values determined from the inflection point in Fig. 14a are in good agreement with the minimum in $-\frac{\mathrm{d}\theta}{\mathrm{d}\sigma}$ vs. σ plots in Fig. 14b. The strain-hardening rate in NiTiCu is significantly higher in comparison to NiTi and NiTiFe. Thus, addition of Cu in NiTi SMA increases $\sigma_c$ and delays DRX in Domain-2.

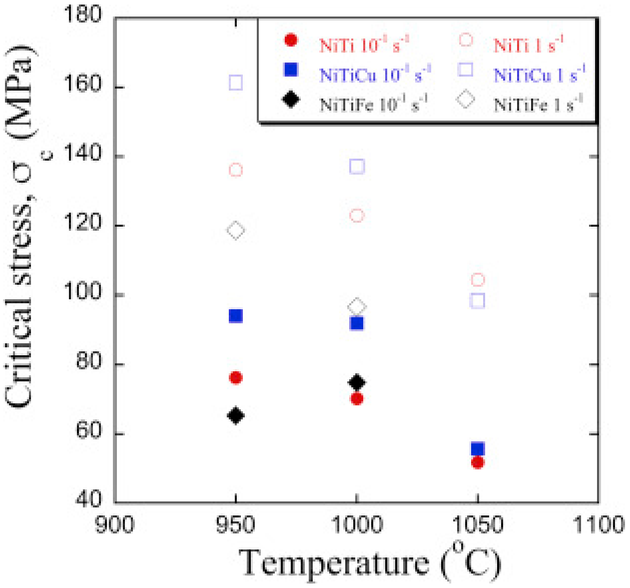


1. Download: Download high-res image (161KB)
2. Download: Download full-size image

Fig. 13. Variation of critical stress, $\sigma_c$, required for the onset of DRX *vs*. operating $T$ and $\dot{\varepsilon}$ range for Domain-2 in NiTi, NiTiCu and NiTiFe SMAs.

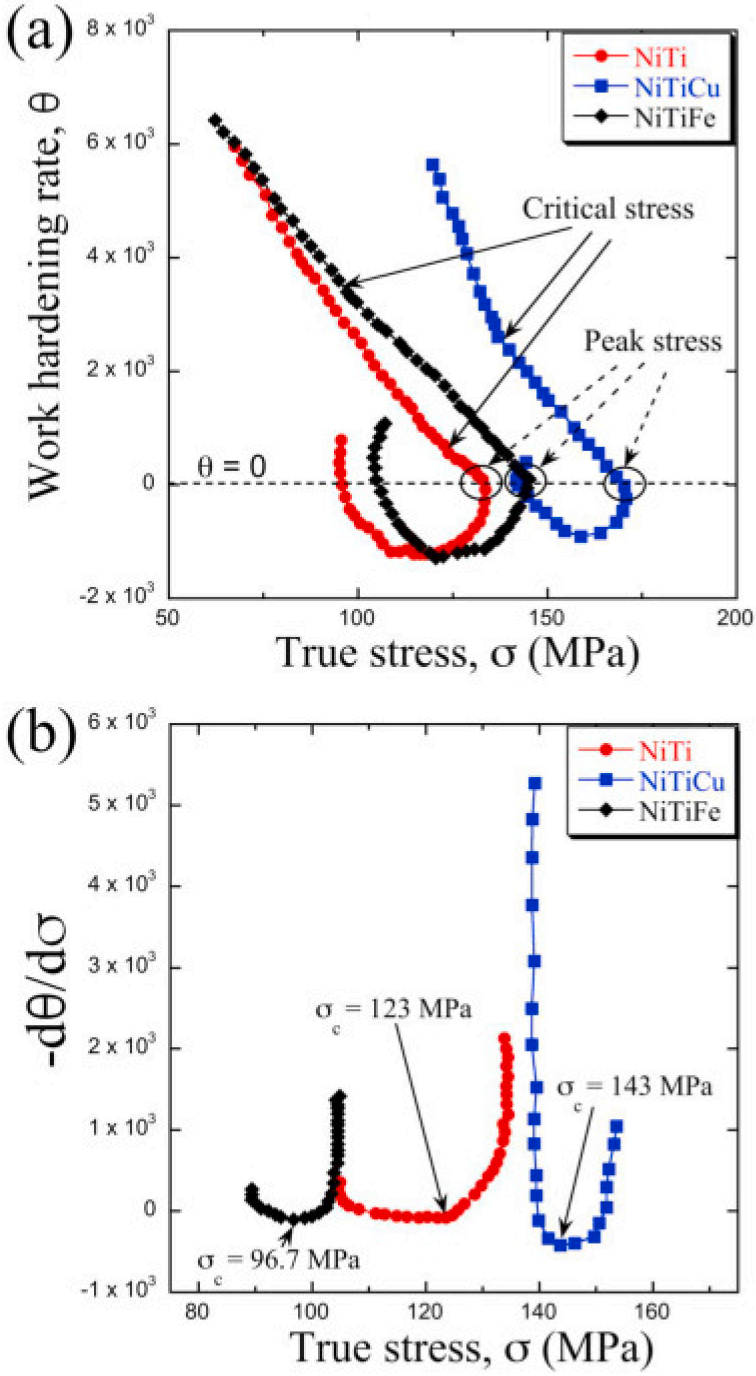


1. Download: Download high-res image (555KB)
2. Download: Download full-size image

Fig. 14. (a) Work hardening rate vs. true stress, (b) -dθdσ vs. true stress plots of NiTi, NiTiCu and NiTiFe SMAs at $T$ = 1000 °C and $\dot{\varepsilon} = 1\ s^{-1}$. Critical stress, $\sigma_c$, for the onset of DRX and peak stress are shown with solid and broken arrows in (a).

## 5. Conclusions

Ternary alloying additions of Fe and Cu on the hot deformation behavior of binary NiTi SMA were investigated using the processing maps approach. Power dissipation, instability and strain rate sensitivity maps have been developed for NiTi, NiTiCu and NiTiFe SMAs based on the data obtained from the hot compression tests performed in the temperature range of 800–1050 °C and with strain rates varying from $10^{-3}$ to $10^{+1}$ $s^{-1}$. Following conclusions are drawn from this study:

1. True stress-true strain curves exhibit flow softening after an initial broad peak stress (at lower $\varepsilon < 0.05$) followed by steady state behavior for specimens tested at all the temperatures and $\dot{\varepsilon} \leq 1$ $s^{-1}$. The flow stress of the SMAs is highly sensitive to strain rate and temperature. Addition of Cu and Fe increases its flow stress and work hardening rate over binary NiTi SMA.
2. Based on the processing maps, addition of Cu in NiTi SMA improves its hot workability through enlarging stable domains for processing whereas Fe addition shrinks it. The flow instability regions increased with Fe addition in binary NiTi SMA. Although Cu extends stable hot working zones for deformation, the extent of applied strain $\varepsilon = 0.7$ was insufficient to induce complete DRX microstructure. This was also evident from the high values of $Z$ and $Q$ in NiTiCu SMA.
3. Domain-2 was identified as the optimum zone for processing of the SMAs with efficiency of power dissipation in the range $\eta$ = 30–45%. Domain-2 in NiTi, NiTiCu and NiTiFe SMAs occurred at $T$ = 950–1050 °C/ $\dot{\varepsilon} = 10^{-1}$ to $10^{+0.5}$ $s^{-1}$, $T$ = 925–1050 °C/ $\dot{\varepsilon} = 10^{-1.5}$ to $10^{+0.5}$ $s^{-1}$ and $T$ = 925–1000 °C/ $\dot{\varepsilon} = 10^{-1}$ to $10^{+0.5}$ $s^{-1}$ respectively. Estimated $\eta$ and $m$ values along with microstructural analysis of the specimens deformed in Domain-2 revealed DRX as the dominating deformation mechanism in NiTi, NiTiFe SMAs and DRV in NiTiCu.
4. Flow instability regions in the processing maps developed on the basis of continuum instability criterion revealed instability in the form of flow localization. The extent of flow localization was found to be significant at higher strain rates.
5. The sluggish DRX kinetics in NiTiCu SMA in Domain-2 is also supported by the higher critical stress, $\sigma_c$, required for the onset of DRX vis-à-vis NiTi, NiTiFe SMAs. The $\sigma_c$ required for the onset of DRX in Domain-2 decreases with increasing deformation temperature and decreasing strain rate.

## Declaration of competing interest

The authors declare that they have no known competing financial interests or personal relationships that could have appeared to influence the work reported in this paper.

## Acknowledgements

The work at Nanyang Technological University was supported by the funding from A*STAR via the Structural Metals and Alloys Programme (No. A18B1b0061).

## Appendix A. Supplementary data

The following is the Supplementary data to this article:

Download: Download Word document (8MB)

Multimedia component 1.

## Authorship statement

All the authors in this work have made substantial contribution to the manuscript. Concept and design of study: S.V.S. Narayana Murty, P. Ramesh Narayan, M. Mohan, P. V. Venkitakrishnan. Analysis and Interpretation of Data, Performed experiments: Gaurav Singh. Drafting of manuscript: Gaurav Singh, Neeraj Nayan and U. Ramamurty.

# References

[1]

K. Otsuka, X. Ren

Physical metallurgy of Ti–Ni-based shape memory alloys

Prog. Mater. Sci., 50 (2005), pp. 511-678

View PDFView articleView in ScopusGoogle Scholar

[2]

T.W. Duerig, K.N. Melton, D. Stöckel

Engineering Aspects of Shape Memory Alloys

Butterworth-Heinemann, London (2013)

Google Scholar

[3]

K. Otsuka, C.M. Wayman

Shape Memory Materials

Cambridge university press (1999)

Google Scholar

[4]

D.J. Hartl, D.C. Lagoudas

Aerospace applications of shape memory alloys

Proc. Inst. Mech. Eng. Part G J. Aerosp. Eng., 221 (2007), pp. 535-552

View in ScopusGoogle Scholar

[5]

J. Van Humbeeck

Non-medical applications of shape memory alloys

Mater. Sci. Eng., 273 (1999), pp. 134-148

View PDFView articleView in ScopusGoogle Scholar

[6]

K.C. Atli, I. Karaman, R.D. Noebe, D. Gaydosh

The effect of training on two-way shape memory effect of binary NiTi and NiTi based ternary high temperature shape memory alloys

Mater. Sci. Eng., 560 (2013), pp. 653-666

View PDFView articleView in ScopusGoogle Scholar

[7]

G. Bozzolo, R.D. Noebe, H.O. Mosca

Site preference of ternary alloying additions to NiTi: Fe, Pt, Pd, Au, Al, Cu, Zr and Hf

J. Alloys Compd., 389 (2005), pp. 80-94

View PDFView articleView in ScopusGoogle Scholar

[8]

G.S. Firstov, J. Van Humbeeck, Y.N. Koval

High temperature shape memory alloys problems and prospects

J. Intell. Mater. Syst. Struct., 17 (2006), pp. 1041-1047

View in ScopusGoogle Scholar

[9]

G.S. Firstov, J. Van Humbeeck, Y.N. Koval

High-temperature shape memory alloys: some recent developments

Mater. Sci. Eng., 378 (2004), pp. 2-10

View PDFView articleView in ScopusGoogle Scholar

[10]

J. Ma, I. Karaman, R.D. Noebe

High temperature shape memory alloys

Int. Mater. Rev., 55 (2010), pp. 257-315

Google Scholar

[11]

A. Nespoli, E. Villa, S. Besseghini

Characterization of the martensitic transformation in $Ni_{50-x}Ti_{50}Cu_x$ alloys through pure thermal measurements
J. Alloys Compd., 509 (2011), pp. 644-647
View PDFView articleView in ScopusGoogle Scholar

[12]

Y.X. Tong, P.C. Jiang, F. Chen, B. Tian, L. Li, Y.F. Zheng, D. V Gunderov, R.Z. Valiev

Microstructure and martensitic transformation of an ultrafine-grained TiNiNb shape memory alloy processed by equal channel angular pressing

Intermetallics, 49 (2014), pp. 81-86

View PDFView articleView in ScopusGoogle Scholar

[13]

N. El-Bagoury

Microstructure and martensitic transformation and mechanical properties of cast Ni rich NiTiCo shape memory alloys

Mater. Sci. Technol., 30 (2014), pp. 1795-1800

View in ScopusGoogle Scholar

[14]

M. Kök, H.S.A. Zardawi, I.N. Qader, M.S. Kanca

The effects of cobalt elements addition on $Ti_2Ni$ phases, thermodynamics parameters, crystal structure and transformation temperature of NiTi shape memory alloys
Eur. Phys. J. Plus., 134 (2019), p. 197
View in ScopusGoogle Scholar

[15]

H. Sehitoglu, I. Karaman, X. Zhang, A. Viswanath, Y. Chumlyakov, H.J. Maier

Strain–temperature behavior of NiTiCu shape memory single crystals

Acta Mater., 49 (2001), pp. 3621-3634

View PDFView articleView in ScopusGoogle Scholar

[16]

T. Kotil, H. Sehitoglu, H.J. Maier, Y.I. Chumlyakov

Transformation and detwinning induced electrical resistance variations in NiTiCu

Mater. Sci. Eng., 359 (2003), pp. 280-289

View PDFView articleView in ScopusGoogle Scholar

[17]

T.H. Nam, T. Saburi, K. Shimizu

Cu-content dependence of shape memory characteristics in Ti–Ni–Cu alloys

Mater. Trans., JIM, 31 (1990), pp. 959-967

CrossrefView in ScopusGoogle Scholar

[18]

T.H. Nam, T. Saburi, K. Shimizu

Effect of thermo-mechanical treatment on shape memory characteristics in a Ti-40Ni-10Cu (at%) alloy

Mater. Trans., JIM, 32 (1991), pp. 814-820

CrossrefView in ScopusGoogle Scholar

[19]

W. Tang, R. Sandström, Z.G. Wei, S. Miyazaki

Experimental investigation and thermodynamic calculation of the Ti-Ni-Cu shape memory alloys

Metall. Mater. Trans., 31 (2000), pp. 2423-2430

CrossrefView in ScopusGoogle Scholar

[20]

M. Es-Souni, M. Es-Souni, H.F. Brandies

On the transformation behaviour, mechanical properties and biocompatibility of two NiTi-based shape memory alloys: NiTi42 and NiTi42Cu7

Biomaterials, 22 (2001), pp. 2153-2161

View PDFView articleView in ScopusGoogle Scholar

[21]

T. Saburi, T. Takagaki, S. Nenno, K. Koshino

Mechanical behavior of shape memory Ti--Ni--Cu alloys

Proc. MRS Int. Meet. Adv. Mater. (1988), pp. 147-152

Google Scholar

[22]

N. Kaur, D. Kaur

NiTiCu/AlN/NiTiCu shape memory thin film heterostructures for vibration damping in MEMS

J. Alloys Compd., 590 (2014), pp. 116-124

View PDFView articleView in ScopusGoogle Scholar

[23]

D.C. Lagoudas, D.A. Miller, L. Rong, P.K. Kumar

Thermomechanical fatigue of shape memory alloys

Smart Mater. Struct., 18 (2009), Article 85021

Google Scholar

[24]

K. Tsuji, Y. Takegawa, K. Kojima

Thermal fatigue characteristics of Ni-Ti-Cu alloy coils

Mater. Sci. Eng., 136 (1991), pp. L1-L4

View PDFView articleView in ScopusGoogle Scholar

[25]

C. Grossmann, J. Frenzel, V. Sampath, T. Depka, G. Eggeler

Elementary transformation and deformation processes and the cyclic stability of NiTi and NiTiCu shape memory spring actuators

Metall. Mater. Trans., 40 (2009), p. 2530

View at publisherCrossrefView in ScopusGoogle Scholar

[26]

M. Matsuda, R. Yamashita, S. Tsurekawa, K. Takashima, M. Mitsuhara , M. Nishida

Antiphase boundary-like structure of B19′ martensite via R-phase transformation in Ti–Ni–Fe alloy

J. Alloys Compd., 586 (2014), pp. 87-93

View PDFView articleView in ScopusGoogle Scholar

[27]

S. Xue, W. Wang, D. Wu, Q. Zhai, H. Zheng

On the explanation for the time-dependence of B2 to R martensitic transformation in $Ti_{50}Ni_{47}Fe_3$ shape memory alloy
Mater. Lett., 72 (2012), pp. 119-121
View PDFView articleView in ScopusGoogle Scholar

[28]

R. Basu, M. Eskandari, L. Upadhayay, M.A. Mohtadi-Bonab, J.A. Szpunar

A systematic investigation on the role of microstructure on phase transformation behavior in Ni–Ti–Fe shape memory alloys

J. Alloys Compd., 645 (2015), pp. 213-222

View PDFView articleView in ScopusGoogle Scholar

[29]

V.B. Krishnan, R.M. Manjeri, B. Clausen, D.W. Brown, R. Vaidyanathan

Analysis of neutron diffraction spectra acquired in situ during mechanical loading of shape memory NiTiFe at low temperatures

Mater. Sci. Eng., 481 (2008), pp. 3-10

View PDFView articleView in ScopusGoogle Scholar

[30]

S.K. Giri, M. Krishnan, U. Ramamurty

Enhancement of fatigue life of Ni–Ti–Fe shape memory alloys by thermal cycling

Mater. Sci. Eng., 528 (2010), pp. 363-370

View PDFView articleView in ScopusGoogle Scholar

[31]

V.B. Krishnan, S.B. Shmalo, C.R. Rathod, M.A.M. Bourke, R. Vaidyanathan

Low temperature deformation of the R-phase in a NiTiFe shape memory alloy

Appl. Phys. Lett., 97 (2010), Article 91910

Google Scholar

[32]

S.Y. Jiang, Y.Q. Zhang, Y.N. Zhao

Dynamic recovery and dynamic recrystallization of NiTi shape memory alloy under hot compression deformation

Trans. Nonferr. Metals Soc. Chin., 23 (2013), pp. 140-147

View PDFView articleView in ScopusGoogle Scholar

[33]

K. Dehghani, A.A. Khamei

Hot deformation behavior of 60Nitinol ($Ni_{60\ wt\%}$-$Ti_{40\ wt\%}$) alloy: experimental and computational studies

Mater. Sci. Eng., 527 (2010), pp. 684-690

View PDFView articleView in ScopusGoogle Scholar

[34]

A.A. Khamei, K. Dehghani

Modeling the hot-deformation behavior of $Ni_{60\ wt\%}$-$Ti_{40\ wt\%}$ intermetallic alloy
J. Alloys Compd., 490 (2010), pp. 377-381
View PDFView articleView in ScopusGoogle Scholar

[35]

M. Morakabati, S. Kheirandish, M. Aboutalebi, A.K. Taheri, S.M. Abbasi

A study on the hot workability of wrought NiTi shape memory alloy

Mater. Sci. Eng., 528 (2011), pp. 5656-5663

View PDFView articleView in ScopusGoogle Scholar

[36]

M. Morakabati, M. Aboutalebi, S. Kheirandish, A. Karimi Taheri, S.M. Abbasi

High temperature deformation and processing map of a NiTi intermetallic alloy

Intermetallics, 19 (2011), pp. 1399-1404

View PDFView articleView in ScopusGoogle Scholar

[37]

S.Y. Jiang, Y.Q. Zhang, Microstructure evolution and deformation behavior of as-cast NiTi shape memory alloy under compression, Trans. Nonferr. Metals Soc. Chin. 90–96.
Google Scholar

[38]

S.Y. Jiang, Y.Q. Zhang, Y.N. Zhao, M. Tang, W.L. Yi

Constitutive behavior of Ni-Ti shape memory alloy under hot compression

J. Cent. South Univ., 20 (2013), pp. 24-29

CrossrefGoogle Scholar

[39]

H. Mirzadeh, M.H. Parsa

Hot deformation and dynamic recrystallization of NiTi intermetallic compound

J. Alloys Compd., 614 (2014), pp. 56-59

View PDFView articleView in ScopusGoogle Scholar

[40]

J.T. Yeom, J.H. Kim, J.K. Hong, S.W. Kim, C.H. Park, T.H. Nam, K.Y. Lee

Hot forging design of as-cast NiTi shape memory alloy

Mater. Res. Bull., 58 (2014), pp. 234-238

View PDFView articleView in ScopusGoogle Scholar

[41]

X. Shu, S. Lu, K. Wang, G. Li

Optimization of hot working parameters of as-forged Nitinol 60 shape memory alloy using processing maps

Met. Mater. Int., 21 (2015), pp. 726-733

CrossrefView in ScopusGoogle Scholar

[42]

V.V. Shastry, B. Maji, M. Krishnan, U. Ramamurty

High-temperature deformation processing maps for a NiTiCu shape memory alloy

J. Mater. Res., 26 (2011), pp. 2484-2492

CrossrefView in ScopusGoogle Scholar

[43]

M. Morakabati, M. Aboutalebi, S. Kheirandish, A.K. Taheri, S.M. Abbasi

Hot tensile properties and microstructural evolution of as cast NiTi and NiTiCu shape memory alloys

Mater. Des., 32 (2011), pp. 406-413

View PDFView articleView in ScopusGoogle Scholar

[44]

Y. Zhang, S. Jiang, C. Chen, L. Hu, X. Zhu

Hot workability of a NiTiCu shape memory alloy with acicular martensite phase based on processing maps

Intermetallics, 86 (2017), pp. 94-103

View PDFView articleGoogle Scholar

[45]

M. Morakabati, S. Kheirandish, M. Aboutalebi, A.K. Taheri, S.M. Abbasi

The effect of Cu addition on the hot deformation behavior of NiTi shape memory alloys

J. Alloys Compd., 499 (2010), pp. 57-62

View PDFView articleView in ScopusGoogle Scholar

[46]

R. Basu, L. Jain, B. Maji, M. Krishnan

Dynamic recrystallization in a Ni-Ti-Fe shape memory alloy: effects on austenite-martensite phase transformation

J. Alloys Compd., 639 (2015), pp. 94-101

View PDFView articleView in ScopusGoogle Scholar

[47]

S. Wang, X. Mi, X. Yin, Y. Li

Deformation behavior of TiNiFe alloy in isothermal compression

Rare Met., 31 (2012), pp. 323-327

Google Scholar

[48]

Y.V.R. K Prasad, K.P. Rao, S. Sasidhar

Hot Working Guide: a Compendium of Processing Maps

ASM international, Materials Park, Ohio (2015)

Google Scholar

[49]

S.V.S. Narayana Murty, B.N. Rao

On the dynamic material model for the hot deformation of materials

J. Mater. Sci. Lett., 18 (1999), pp. 1757-1758

Google Scholar

[50]

S.V.S. Narayana Murty, B.N. Rao, B.P. Kashyap

On the hot working characteristics of 6061Al–SiC and 6061–Al 2 O 3 particulate reinforced metal matrix composites

Compos. Sci. Technol., 63 (2003), pp. 119-135

View PDFView articleView in ScopusGoogle Scholar

[51]

C. Yu, G. Kang, X. Xie, W. Rao

A micromechanical model for the grain size dependent super-elasticity degeneration of NiTi shape memory alloys

Mech. Mater., 125 (2018), pp. 35-51

View PDFView articleView in ScopusGoogle Scholar

[52]

A. Biswas, G. Singh, S.K. Sarkar, M. Krishnan, U. Ramamurty

Hot deformation behavior of Ni-Fe-Ga-based ferromagnetic shape memory alloy - a study using processing map

Intermetallics, 54 (2014), pp. 69-78

View PDFView articleView in ScopusGoogle Scholar

[53]

N. Nayan, G. Singh, S.V.S. Narayana Murty, A.K. Jha, B. Pant, K.M. George, U. Ramamurty

Hot deformation behaviour and microstructure control in AlCrCuNiFeCo high entropy alloy

Intermetallics, 55 (2014), pp. 145-153

View PDFView articleView in ScopusGoogle Scholar

[54]

N. Nayan, G. Singh, S.V.S. Narayana Murty, A.K. Jha, B. Pant, K.M. George

High-temperature deformation processing map approach for obtaining the desired microstructure in a multi-component ( Ni-Ti-Cu-Fe ) alloy

Metall. Mater. Trans., 46 (2015), pp. 2201-2215

CrossrefView in ScopusGoogle Scholar

[55]

G. Bajargan, G. Singh, U. Ramamurty

Effect of Li addition on the optimum thermo-mechanical processing parameters of the Mg alloy AZ31

Metall. Mater. Trans. A Phys. Metall. Mater. Sci., 48 (2017), pp. 4262-4274

CrossrefView in ScopusGoogle Scholar

[56]

I. Sen, R.S. Kottada, U. Ramamurty

High temperature deformation processing maps for boron modified Ti–6Al–4V alloys

Mater. Sci. Eng., 527 (2010), pp. 6157-6165

View PDFView articleView in ScopusGoogle Scholar

[57]

G. Singh, U. Ramamurty

Boron modified titanium alloys

Prog. Mater. Sci., 111 (2020), Article 100653

View PDFView articleView in ScopusGoogle Scholar

[58]

Y.V.R. K Prasad

Recent advances in the science of mechanical processing

Indian J. Technol., 28 (1990), pp. 435-451

Google Scholar

[59]

Y.V.R. K
Prasad, H.L. Gegel, S.M. Doraivelu, J.C. Malas, J.T. Morgan, K.A. Lark
, D.R. Barker

Modeling of dynamic material behavior in hot deformation: forging of Ti-6242

Metall. Trans. A., 15 (1984), pp. 1883-1892

Google Scholar

[60]

S.V.S. Narayana Murty, B. Nageswara Rao

On the development of instability criteria during hotworking with reference to IN 718

Mater. Sci. Eng., 254 (1998), pp. 76-82

View in ScopusGoogle Scholar

[61]

S.V.S. Narayana Murty, B.N. Rao

On the flow localization concepts in the processing maps of IN718

Mater. Sci. Eng., 267 (1999), pp. 159-161

Google Scholar

[62]

J. Frenzel, E.P. George, A. Dlouhy, C. Somsen, M.F.X. Wagner, G. Eg
geler

Influence of Ni on martensitic phase transformations in NiTi shape memory alloys

Acta Mater., 58 (2010), pp. 3444-3458

View PDFView articleView in ScopusGoogle Scholar

[63]

M.O. Bodunrin

Flow stress prediction using hyperbolic-sine Arrhenius constants optimised by simple generalised reduced gradient refinement

J. Mater. Res. Technol., 9 (2020), pp. 2376-2386

View PDFView articleView in ScopusGoogle Scholar

[64]

S.M. Oppenheimer, A.R. Yung, D.C. Dunand

Power-law creep in near-equiatomic nickel-titanium alloys

Scripta Mater., 57 (2007), pp. 377-380

View PDFView articleView in ScopusGoogle Scholar

[65]

S. Jiang, D. Sun, Y. Zhang, L. Hu

Deformation behavior and microstructure evolution of NiTiCu shape memory alloy subjected to plastic deformation at high temperatures

Metals, 7 (2017), pp. 294-304

CrossrefView in ScopusGoogle Scholar

[66]

A. Shamsolhodaei, A. Zarei-Hanzaki, M. Ghambari, S. Moemeni

The high temperature flow behavior modeling of NiTi shape memory alloy employing phenomenological and physical based constitutive models: a comparative study

Intermetallics, 53 (2014), pp. 140-149

View PDFView articleView in ScopusGoogle Scholar

[67]

F.J. Humphreys, M. Hatherly

Recrystallization and Related Annealing Phenomena

Elsevier, New York (2012)

Google Scholar

[68]

Y.V.R.K. Prasad, S. Sasidhara, V.K. Sikka

Characterization of mechanisms of hot deformation of as-cast nickel aluminide alloy

Intermetallics, 8 (2000), pp. 987-995

View PDFView articleView in ScopusGoogle Scholar

[69]

A. Najafizadeh, J.J. Jonas

Predicting the critical stress for initiation of dynamic recrystallization

ISIJ Int., 46 (2006), pp. 1679-1684

CrossrefView in ScopusGoogle Scholar

[70]

H. Mirzadeh, A. Najafizadeh

Hot deformation and dynamic recrystallization of 17-4 PH stainless steel

ISIJ Int., 53 (2013), pp. 680-689

View at publisherCrossrefView in ScopusGoogle Scholar

[71]

H. Mirzadeh, J.M. Cabrera, J.M. Prado, A. Najafizadeh

Hot deformation behavior of a medium carbon microalloyed steel

Mater. Sci. Eng., 528 (2011), pp. 3876-3882

View PDFView articleView in ScopusGoogle Scholar